THE JOURNAL OF PHYSICAL CHEMISTRY B

pubs.acs.org/JPCB Article

Molecular Dynamics Simulations, Reaction Pathway and Mechanism Dissection, and Kinetics Modeling of the Nitric Acid Oxidation of Dicyanamide and Dicyanoborohydride Anions

Wenjing Zhou, Jianbo Liu,* Steven D. Chambreau, and Ghanshyam L. Vaghjiani

Cite This: J. Phys. Chem. B 2020, 124, 11175−11188 Read Online

ACCESS | Metrics & More | Article Recommendations | Supporting Information

ABSTRACT: Direct dynamics simulations of HNO_3 with dicyanamide anion DCA^- (*i.e.*, $N(CN)_2^-$) and dicyanoborohydride anion $DCBH^-$ (*i.e.*, $BH_2(CN)_2^-$) were performed at the B3LYP/6-31+G(d) level of theory in an attempt to elucidate the primary and secondary reactions in the two reaction systems. Guided by trajectory results, reaction coordinates and potential energy diagrams were mapped out for the oxidation of DCA^- and $DCBH^-$ by one and two HNO_3 molecules, respectively, in the gas-phase and in the condensed-phase ionic liquids using the B3LYP/6-311++G(d,p) method. The oxidation of DCA^- by HNO_3 is initiated by proton transfer. The most important pathway leads to the formation of $O_2N{-}NHC(O)NCN^-$, and the latter reacts with a second HNO_3 to produce $O_2N{-}NHC(O)NC(O)NH{-}NO_2^-$($DNB^-$). The oxidation of $DCBH^-$ by HNO_3 may follow a similar mechanism as that of DCA^-, producing two analogue products: $O_2N{-}NHC(O)BH_2CN^-$ and $O_2N{-}NHC(O)BH_2C(O)NH{-}NO_2^-$. Moreover, two new, unique reaction pathways were discovered for $DCBH^-$ because of its boron-hydride group: (1) isomerization of $DCBH^-$ to $CNBH_2CN^-$ and $CNBH_2NC^-$ and (2) H_2 elimination in which the proton in HNO_3 combines with a hydride-H in $DCBH^-$. The Rice−Ramsperger−Kassel−Marcus (RRKM) theory was utilized to calculate reaction kinetics and product branching ratios. The RRKM results indicate that the formation of DNB^- is exclusively important in the oxidation of DCA^-, whereas the same type of reaction is a minor channel in the oxidation of $DCBH^-$. In the latter case, H_2 elimination becomes dominating. The RRKM modeling also indicates that the oxidation rate constant of $DCBH^-$ is higher than that of DCA^- by an order of magnitude. This rationalizes the enhanced preignition performance of $DCBH^-$ over DCA^- with HNO_3.

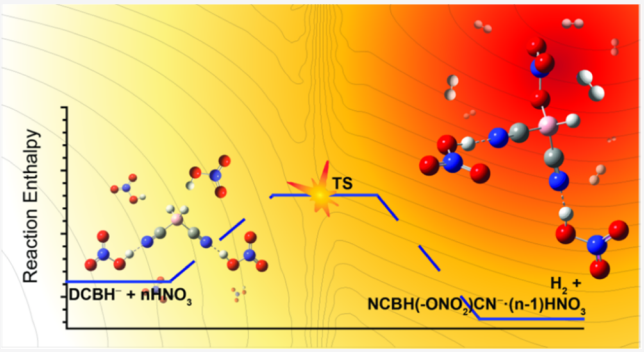

1. INTRODUCTION

In addition to their applications as explosives, energetic ionic liquids (ILs, the salts with melting point ≤100 °C) have become of interest within the aerospace research community as green propellant alternatives to highly toxic, volatile, and sensitive hydrazine for rocket propulsion applications.[1,2] The so-called hypergolic ILs in this context can ignite spontaneously upon contact with an oxidizer (*e.g.*, HNO_3 and N_2O_4/NO_2) and are expected to present lower vapor toxicities than hydrazine and thus reduce environmental hazards.[1−3] The designability of hypergolic ILs includes the choice of cation and anion within a single ion pair, each of which can be modified independently using a modular strategy.[3] This allows flexibility in customizing IL properties and performance for anticipated purposes.

One direction in the design and synthesis of new hypergolic fuels is to have ignition delay (ID) time (defined as the time between the initial fuel/oxidizer contact and the start of combustion) of less than 5 ms.[1] Studies have shown that anions are directly associated with hypergolicity and play a decisive role during the induction stage of ignition, while cations (such as 1,3-dialkyl-imidazolium[4] and triazolium[5]) tune ILs' physicochemical properties and play only a secondary role in influencing the ID time.[1,6] Dicyanamide anion $N(CN)_2^-$ (designated as DCA^-) and dicyanoborohydride anion $BH_2(CN)_2^-$ (designated as $DCBH^-$) are well known for their hypergolicity in propellant formulations.[1,7,8] DCA^--containing hypergolic ILs were first reported in 2008.[7] The DCA^- anion was chosen because of its high N-content and low viscosity, but the resulting ILs exhibit moderate improvement in ID times. $DCBH^-$-containing hypergolic ILs, reported 3 years later, present remarkably shorter ID times than those containing DCA^-.[8] For comparison, the ID time with 100%

Received: August 27, 2020
Revised: October 28, 2020
Published: November 19, 2020

Downloaded via QUEENS COLG on January 5, 2021 at 15:26:32 (UTC).
See https://pubs.acs.org/sharingguidelines for options on how to legitimately share published articles.

ACS Publications © 2020 American Chemical Society

https://dx.doi.org/10.1021/acs.jpcb.0c07823
J. Phys. Chem. B 2020, 124, 11175−11188

HNO_3 was measured to be 8 ms for 1-allyl-3-methylimidazolium dicyanoborohydride[8] ($AMIM^+DCBH^-$) versus 43 ms for $AMIM^+DCA^-$[7] and 28 ms for 1-butyl-3-methylimidazolium dicyanoborohydride[8] ($BMIM^+DCBH^-$) versus 60 ms for $BMIM^+DCA^-$.[9] The shorter ID times of $DCBH^-$-containing ILs imply that the boron-hydride anion prompts the IL reactions with oxidizers and the propagation toward ignition. This is consistent with the high oxidation reactivity observed in the ILs containing BH_4^-,[10] $Al(BH_4)_4^-$,[2] BH_3CN^-,[11] $BH_3(CN)BH_2(CN)^-$,[12,13] BH_2CN,[14] and borohydride cluster anions[15] and in the amine borane/cyanoborane zwitterionic compounds.[16] Besides, the imidazolium-DCBH ILs possess lower viscosities than their DCA-counterparts (*e.g.*, $AMIM^+DCBH^-$ has the lowest viscosity, 12.4 cP at room temperature,[8] among the known hypergolic ILs), which facilitates the mixing of the IL with an oxidizer and makes ignition and combustion faster.

The ignition of hypergolic ILs with an oxidizer involves two stages, a preignition stage during which exothermic redox reactions lead to formation of gaseous transient species accompanied by the release of heat and the increase of the system's temperature, followed by a stage in which the system temperature reaches the kindling point of the inflammable gaseous species, leading to ignition and subsequent combustion to occur.[1,17] Chambreau *et al.* investigated the preignition of DCA^- with white fuming nitric acid (WFNA) by utilizing infrared spectroscopy[6] and mass spectrometry.[18] They proposed that the preignition reaction is initiated by proton transfer (PT) from HNO_3 to a terminal nitrile N in DCA^-, followed by the addition of NO_3^- to the C* atom in the neutral HNC*NCN and then the migration of NO_2 to the terminal NH *via* a 1,3-shift analogous to the acid-catalyzed hydrolysis of nitriles. The resulting nitrouret species $O_2N{-}NHC(O)NCN^-$ reacts with a second HNO_3, producing the 1,5-dinitrobiuret anion $O_2N{-}NHC(O)NC(O)NH{-}NO_2^-$ (designated as DNB^-). As CO_2, N_2O, and isocyanic acid (HNCO) were detected as the only common preignition products of all heterocyclic-DCA ILs and the thermal decomposition of the neutral HDNB (*i.e.*, $O_2N{-}NHC(O){-}NHC(O)NH{-}NO_2$) produced the same products,[19,20] the formation of DNB^- during the preignition of DCA^- was validated. Chambreau *et al.*'s work was followed by other experimental[21,22] and theoretical studies.[22,23] Nichols *et al.* measured the reaction rate constant of DCA^- with HNO_3 in a selected ion flow tube and calculated the reaction potential energy diagrams for DCA^- reacting with one and two HNO_3 molecules.[22] Vogelhuber *et al.* modeled the cation effects on the hypergolicity of DCA^- and identified lower reaction activation barriers by adding Na^+.[23] Litzinger and Iyer proposed other decomposition pathways of the $O_2N{-}NHC(O)NCN^-$ intermediate in the DCA^- preignition.[21]

Recently, Thomas *et al.* compared the hypergolic reactions of $BMIM^+DCA^-$ and $BMIM^+DCBH^-$ with WFNA.[24] The two ILs generated both common and unique products. The N_2O and NO_2 products were detected in the reactions of both ILs although the concentration of NO_2 was significantly higher in the reaction of $BMIM^+DCBH^-$ than in $BMIM^+DCA^-$. CO_2 and HNCO were produced only in the reaction of $BMIM^+DCA^-$, whereas hydrogen cyanide (HCN) [and/or its isomer hydrogen isocyanide (HNC)] was produced only in the reaction of $BMIM^+DCBH^-$. They also detected the $BH(OH)(CN)_2^-$ anion in the oxidation of $BMIM^+DCBH^-$ by dilute HNO_3. More recently, Brotton and Kaiser[25] performed the hypergolic ignition of $BMIM^+DCA^-$ with diluted HNO_3 by merging two droplets in an acoustic levitator and detected CO_2, N_2O, NO_3^-, organic nitrites, and the carbonyl group in the products.

Although several experimental and theoretical works have been carried out for DCA^-- and $DCBH^-$-based ILs, questions remain about what is responsible for their different ID times and their preignition/ignition kinetics and dynamics. One challenge for experimentalists is in the difficulty to capture *in situ* all of the generated transient species and to distinguish primary and secondary products. As demonstrated in our recent work,[4,5,26] theoretical modeling provides an alternative to experiments for testing and ascertaining the possibilities of various IL ignition mechanisms and the respective roles of different anions. The work presented in this paper sought to investigate and compare the preignition of DCA^- versus $DCBH^-$, including their oxidative capacities, reaction mechanisms, and product channels with HNO_3 by using direct dynamics trajectory simulations,[27−29] reaction coordinate and potential energy computations, and kinetics modeling.

2. METHODOLOGIES OF COMPUTATIONAL MODELING

Direct dynamics simulations of HNO_3 with DCA^- and $DCBH^-$ were carried out using the Venus[30] program to set up initial conditions and the Hessian-based predictor-corrector algorithm,[31] implemented in Gaussian 09,[32] to integrate trajectories. Trajectories started at the lowest energy geometries of HNO_3 and DCA^- (or $DCBH^-$), with initial separation between the centers of mass of the randomly oriented reactants set to 8.0 Å. Reactant vibrational energies (E_{vib}) and modes were sampled using quantum Boltzmann probability distributions at specific temperatures.[33] Reactant rotational energies (E_{rot}) were sampled from classical Boltzmann distributions. Collision energy (E_{col}) was added as relative translational energy. Trajectories were propagated at a step size of 0.25 $amu^{1/2}$·Bohr and terminated after product separation exceeded 8.0 Å. The propagation step size is small enough for SCF convergence as well as to keep the system energy-constant within 10^{-4} Hartree. The B3LYP/6-31+G(d) level of theory was chosen for trajectory simulations as it provided a good description of DCA^- reactions in our previous work.[4,5,26] Representative reaction pathways identified at the B3LYP level were verified using a range-separated functional ωB97XD/6-31+G(d). Details of trajectory simulations are available in the Supporting Information. Trajectory reaction pathways were sorted and trajectory ensembles were analyzed by using in-house custom programs written for these purposes.

To construct reaction coordinates and potential energy diagrams for the trajectory-predicted reaction pathways, structures of the reactants, intermediates, transition states (TSs), and products identified in the trajectories were recalculated at the B3LYP/6-311++G(d,p) level of theory using Gaussian 09 and/or Gaussian 16.[34] Cartesian coordinates for all of the calculated species are provided in the Supporting Information. TSs were verified to be first-order saddle points, with single imaginary vibrational mode that corresponded to the anticipated reaction coordinate. Intrinsic reaction coordinate calculations were carried out to confirm that TSs were located between correct minima. Reaction enthalpies (ΔH) and changes in Gibbs free energy (ΔG) were evaluated at 298 K, including zero-point energies, which were scaled by a factor of 0.981.[35] The resulting reaction potential

https://dx.doi.org/10.1021/acs.jpcb.0c07823
J. Phys. Chem. B 2020, 124, 11175−11188

Table 1. Trajectory Reaction Probabilities (%) for DCA^- + HNO_3 and HDCA + NO_3^- under Various Conditions[a]

temperature/K	1000	2000	3000	4000	5000	
E_{col}/eV	0.5	0.5	0.5	0.5	0.5	intermediate or TS
DCA^- + HNO_3						
PT_{N1}: $N(CN)_2^-$ + HNO_3 → $NCNCN^-{\cdot}HNO_3$	12 ± 3	5 ± 2	15 ± 4	18 ± 4	15 ± 4	$NCNCN^-{\cdot}HNO_3$
PT_{N3}: $N(CN)_2^-$ + HNO_3 → $(CN)_2N^-{\cdot}HNO_3$	0	3 ± 2	2 ± 1	1 ± 1	1 ± 1	$(CN)_2N^-{\cdot}HNO_3$
reversible PT_{N1}: $N(CN)_2^-$ + HNO_3 ⇌ $NCNCN^-{\cdot}HNO_3$	52 ± 5	54 ± 5	28 ± 4	29 ± 5	20 ± 4	$NCNCN^-{\cdot}HNO_3$
reversible PT_{N3}: $N(CN)_2^-$ + HNO_3 ⇌ $(CN)_2N^-{\cdot}HNO_3$	14 ± 3	12 ± 3	17 ± 4	9 ± 3	9 ± 3	$(CN)_2N^-{\cdot}HNO_3$
dissociation: HNO_3 → NO_2 + OH	0	0	1 ± 1	6 ± 2	19 ± 4	HNO_3
dissociation: HNCNCN → HNC + NCN	0	0	0	0	4 ± 2	DCA^-
HDCA + NO_3^-						
PT: HNCNCN + NO_3^- → $NCNCN^-$ + HNO_3	68 ± 5	58 ± 5	57 ± 5	52 ± 5		$NCNCN^-{\cdot}HNO_3$
reversible PT: HNCNCN + NO_3^- ⇌ $NCNCN^-$ + HNO_3	20 ± 4	22 ± 4	16 ± 4	21 ± 4		$NCNCN^-{\cdot}HNO_3$
NO_3 addition: HNCNCN + NO_3^- → $HNC(-ONO_2)NCN^-$	3 ± 2	6 ± 2	6 ± 2	6 ± 2		F1.TS0
NO_2 elimination: $HNC(-ONO_2)NCN^-$→ $[HNC(O)NCN]^{\bullet-}$ + NO_2	0	3 ± 2	2 ± 1	3 ± 2		$HNC(-ONO_2)NCN^-$
dissociation: HNO_3 → NO_2 + OH	0	0	1 ± 1	12 ± 3		HNO_3
dissociation: HDCA → HNC + NCN	0	0	0	3 ± 2		HDCA

[a]Percent probabilities and uncertainties were calculated on the basis of 100 trajectories for each condition. Some trajectories have presented PT and fragmentation simultaneously or sequentially.

Table 2. Trajectory Reaction Probability (%) for $DCBH^-$ + HNO_3 and HDCBH + NO_3^- under Various Conditions[a]

	temperature/K			
$DCBH^-$ + HNO_3 at E_{col} = 0.5 eV	3000	4000	5000	intermediate or TS
PT: $NCBH_2CN^-$ + HNO_3 → $NCBH_2CN^-{\cdot}HNO_3$	4 ± 2	4 ± 2	14 ± 3	$NCBH_2CN^-{\cdot}HNO_3$
reversible PT: $NCBH_2CN^-$ + HNO_3 ⇌ $NCBH_2CN^-{\cdot}HNO_3$	27 ± 4	17 ± 4	4 ± 2	$NCBH_2CN^-{\cdot}HNO_3$
1,2-HT: $NCBH_2CN^-{\cdot}HNO_3$ → $O_3NH{\cdot}NCHBHCN^-$	2 ± 1	0	0	F2.TS4
NO_3 addition to B: $O_3NH{\cdot}NCHBHCN^-$ → $HNCHBH(-ONO_2)CN^-$	1 ± 1	0	0	$O_3NH{\cdot}NCHBHCN^-$
H_2 elimination: $NCBH_2CN^-$ + HNO_3 → H_2 + $NCHB(-ONO_2)CN^-$/$NCHB(-ONO_2)NC^-$	1 ± 1	2 ± 1	3 ± 2	F4.TS0
dissociation: $DCBH^-$ ($NCBH_2CN^-{\cdot}HNO_3$) → BH_2CN + NC^- ($^-O_2NO{\cdot}HNC$)	2 ± 1	3 ± 2	9 ± 3	$DCBH^-$ $NCBH_2CN^-{\cdot}HNO_3$
NO_3 addition to B: BH_2CN + NO_3^- → $BH_2(-ONO_2)CN^-$	1 ± 1	2 ± 1	4 ± 2	BH_2CN
PT: NC^- + HNO_3 → HNC/HCN + NO_3^-	4 ± 2	3 ± 2	9 ± 3	NC^-
dissociation: HNO_3 → NO_2 + OH	1 ± 1	3 ± 2	4 ± 2	HNO_3
	temperature/K			
HDCBH + NO_3^- at E_{col} = 0.5 eV	1000	2000	3000	intermediate or TS
PT: $HNCBH_2CN$ + NO_3^- → $NCBH_2CN^-$ + HNO_3	98 ± 1	81 ± 4	60 ± 5	$NCBH_2CN^-{\cdot}HNO_3$
PT: $HNCBH_2CN$ + NO_3^- → $HNCBHCN^-$ + HNO_3	0	3 ± 2	3 ± 2	F2.TS6
1,2-HT followed by NO_3 addition to B: $HNCBH_2CN$ + NO_3^- → $HNCHBH(-ONO_2)CN^-$	1 ± 1	4 ± 2	9 ± 3	F2.TS4
NO_3 addition to C: $HNCBH_2CN$ + NO_3^-→ $HNC(-ONO_2)BH_2CN^-$	3 ± 1	2 ± 1	0	F2.TS0
dissociation: HDCBH/$DCBH^-$ → HNC/NC^- + BH_2CN	0	2 ± 1	20 ± 4	HDCBH/$DCBH^-$
NO_3 addition to B: BH_2CN + NO_3^- → $BH_2(-ONO_2)CN^-$	0	3 ± 2	11 ± 3	BH_2CN

[a]Percent probabilities and uncertainties were calculated on the basis of 100 trajectories for each condition. Some trajectories have presented multiple reactions simultaneously or sequentially.

energy diagrams were used for kinetics modeling based on the Rice−Ramsperger−Kassel−Marcus (RRKM) theory,[36] for which the program of Zhu and Hase[37] was utilized.

To simulate the reactions in a condensed-phase IL environment, important reaction pathways were recalculated using a parameterized SCRF-base SMD method[38] (often referred to as the generic ILs solvation model, SMD-GIL) with solvent parameters that were consistent with the experiment.

3. TRAJECTORY SIMULATION RESULTS

3.1. DCA^- + HNO_3. We first simulated the bimolecular collisions of DCA^- with HNO_3 at five different temperatures ranging from 1000 to 5000 K and E_{col} = 0.5 eV, and 100 trajectories were calculated for each initial condition. The simulation temperatures and E_{col} were chosen to accelerate and observe reactions on a reasonable timescale but not overwhelmingly decompose the reactants within the trajectory integration time (up to ∼3 ps). For this reason, the simulation temperatures are high and do not indicate the actual temperatures in real rocket motors.[17] At high simulation temperatures, trajectories may find reaction pathways with activation barriers too high to be of relevance to the realistic conditions. The idea is that, with enough trajectories, all possible pathways could be identified including those that control reactions under the conditions of interest. Once these pathways are found, their reaction intermediates, TSs, and potential energy surfaces (PESs) can be calculated. Only those being able to contribute significantly to the preignition and ignition kinetics need to be considered. Another advantage of using high simulation temperatures and E_{col} is that reactants are vigorously excited in the trajectories because of both high E_{vib} and ion−molecule collisions. Consequently, the simulations are able to explore all energetically accessible structures and all of the various reactant conformers can form and

https://dx.doi.org/10.1021/acs.jpcb.0c07823
J. Phys. Chem. B 2020, 124, 11175−11188

contribute to the trajectory outcomes although the trajectories are being initiated at the single lowest energy reactant conformation.

The trajectory results are summarized in the first part of Table 1. The first two reaction pathways correspond to PT from HNO_3 to a terminal nitrile N atom (referred to as PT_{N1}) and the central N atom in DCA^- (referred to as PT_{N3}), respectively. PT_{N1} represents a major product channel. It accounts for a percent yield of 12% at 1000 K and 15% at 5000 K. PT_{N3}, on the other hand, appears to be minor. A large fraction of trajectories underwent reversible PT_{N1} and PT_{N3}. These trajectories were counted as nonreactive as long as the trajectories returned to their starting structures by the end of the simulation. Fragmentation of $HNO_3 \rightarrow NO_2 + OH$ and of the neutral HDCA product (*i.e.*, HNCNCN) → HNC + cyanonitrene (N≡CN) started to emerge in the trajectories at a temperature higher than 3000 K. Our trajectory prediction is consistent with Chambreau *et al.*'s finding[6] that PT_{N1} is the first step in the preignition of DCA^-. This result has thus motivated us to simulate the collisions of the neutral HDCA molecule with NO_3^-.

3.2. HDCA + NO_3^-. A batch of 100 trajectories was computed for each of the four initial conditions specified in the second part of Table 1. One common pathway corresponds to the transfer of a proton from HDCA back to NO_3^-, which has maintained a probability of >50% throughout the whole temperature range. However, the mechanistically most interesting pathway corresponds to the formation of an intermediate complex $HNC(-ONO_2)NCN^-$, a significant fraction of which are followed by NO_2 elimination to produce $[HNC(O)NCN]^{\bullet-}$. A representative trajectory is demonstrated in Figure S1 in the Supporting Information. In this trajectory, the collision occurs at 285 fs (indicated by the complete E_{col} → internal energy conversion and the formation of a new rC−O bond at that time). The intermediate lasts for 125 fs until the elimination of NO_2 occurs at 410 fs, as indicated by the breaking rO−NO_2 bond.

Similar to the trajectories of $DCA^- + HNO_3$, the thermal decomposition of HNO_3 and HDCA was observed only at elevated temperatures.

3.3. $DCBH^- + HNO_3$. A preliminary test has shown that the collisions of $DCBH^-$ with HNO_3 simulated at 1000−2000 K are mostly nonreactive within the trajectory time (~3 ps). Therefore, the main set of trajectories was simulated at 3000, 4000, and 5000 K (100 trajectories at each temperature). A total of nine reaction pathways were identified in the trajectories, including both primary and secondary reactions. They are reported in the first section of Table 2.

Similar to $DCA^- + HNO_3$, the PT from HNO_3 to a terminal N atom in $DCBH^-$ represents a large fraction of the reactive trajectories for $DCBH^- + HNO_3$, and many of the PT trajectories are reversible. The $NCBH_2CN^-{\cdot}HNO_3$ product appears to be a hydrogen-bonded complex with the proton located closer to the NO_3^- anion (as in $NCNCN^-{\cdot}HNO_3$). $NCBH_2CN^-{\cdot}HNO_3$ may undergo a 1,2-H atom shift from the boron to a neighboring C and isomerize to $O_3NH{\cdot}NCHBHCN^-$. The NO_3^- moiety may then attack the electrophilic boron, forming an $HNCHBH(-ONO_2)CN^-$ complex. Figure S2a in the Supporting Information demonstrates a trajectory that goes through all of the three reactions

$$NCBH_2CN^- + HNO_3 \xrightarrow{①} NCBH_2CN^-{\cdot}HNO_3 \xrightarrow{②}$$

$$O_3NH{\cdot}NCHBHCN^- \xrightarrow{③} HNCHBH(-ONO_2)CN^-$$

each of which is manifested by the changes in the potential and translational energies and in the respective chemical bonds.

The PT reaction may accompany elimination of an HNC molecule. The remaining BH_2CN reacts with NO_3^- to form a $BH_2(-ONO_2)CN^-$ intermediate, as illustrated by the trajectory of

$$NCBH_2CN^- + HNO_3 \xrightarrow{①} NCBH_2CN^-{\cdot}HNO_3 \xrightarrow{②}$$

$$BH_2CN + O_2NO^-{\cdot}HNC \xrightarrow{③} BH_2(-ONO_2)CN^- + HNC$$

in Figure S2b of the Supporting Information.

Equally interesting reaction pathways are the BH_2-mediated H_2 elimination, as exemplified by Figure S2c,d in the Supporting Information. The trajectory in Figure S2c demonstrates a straightforward H_2-elimination mechanism where the proton in HNO_3 approaches and combines with a hydride-H at boron to form an H_2 molecule; the remaining NO_3 is attracted to the boron atom, forming an $NCBH(-ONO_2)CN^-$ complex. An alternative and more convoluted pathway is shown in Figure S2d, where the reaction is initiated by the HNO_3-induced isomerization of $NCBH_2CN^-$ to $CNBH_2CN^-$ (step ①), followed by H_2 elimination (step ②) and then the binding of NO_3^- to the B atom (step ③). Finally, $CNBH(-ONO_2)CN^-$ eliminates a CN^- anion (step ④) and then an NO_2 molecule (step ⑤).

As the simulation temperature increased, the decomposition of $DCBH^-$ (and $DCBH^-{\cdot}HNO_3$) to BH_2CN and CN^- (and HNC) became severe, as the decomposition of HNO_3. The BH_2CN product may react with NO_3^-, as described above. The CN^- anion may abstract a proton from HNO_3, producing HNC and/or HCN.

3.4. HDCBH + NO_3^-. Inspired by the finding that intermolecular PT represents an initial step in most of the $DCBH^- + HNO_3$ reaction pathways, we have further simulated the direct dynamics of HDCBH (*i.e.*, $HNCBH_2CN$) with NO_3^-. Hundred trajectories were accumulated under each of the three initial conditions described in the second section of Table 2. The overwhelmingly dominant pathway is back PT from the terminal NH to NO_3^-, that is, $HDCBH + NO_3^- \rightarrow DCBH^- + HNO_3$. In addition, the PT from BH_2 to NO_3^- was observed, that is, $HNCBH_2CN + NO_3^- \rightarrow HNCBHCN^- + HNO_3$, with a small probability (only 3%).

Compared to the trajectories of $DCBH^- + HNO_3$ starting under the same initial conditions, the trajectories of $HDCBH + NO_3^-$ have shown enhanced probabilities for a 1,2-H shift in $HNCBH_2CN$ and for the formation of $HNCHBH(-ONO_2)CN^-$ and $BH_2(-ONO_2)CN^-$. In addition, NO_3^- may attack the carbon atom in HDCBH and form $HNC(-ONO_2)BH_2CN^-$ (*i.e.*, an analogue of $HNC(-ONO_2)NCN^-$ that forms in the reaction of $HDCA + NO_3^-$). However, the formation probability for $HNC(-ONO_2)BH_2CN^-$ (at most 3%) is lower than that for $HNC(-ONO_2)NCN^-$ (6%).

4. REACTION COORDINATES AND POTENTIAL ENERGY DIAGRAMS FOR TRAJECTORY-PREDICTED PATHWAYS

4.1. Reaction of DCA^- with HNO_3. *4.1.1. Reaction Pathways Initiated by PT_{N1}.* The trajectory results have

https://dx.doi.org/10.1021/acs.jpcb.0c07823
J. Phys. Chem. B 2020, 124, 11175−11188

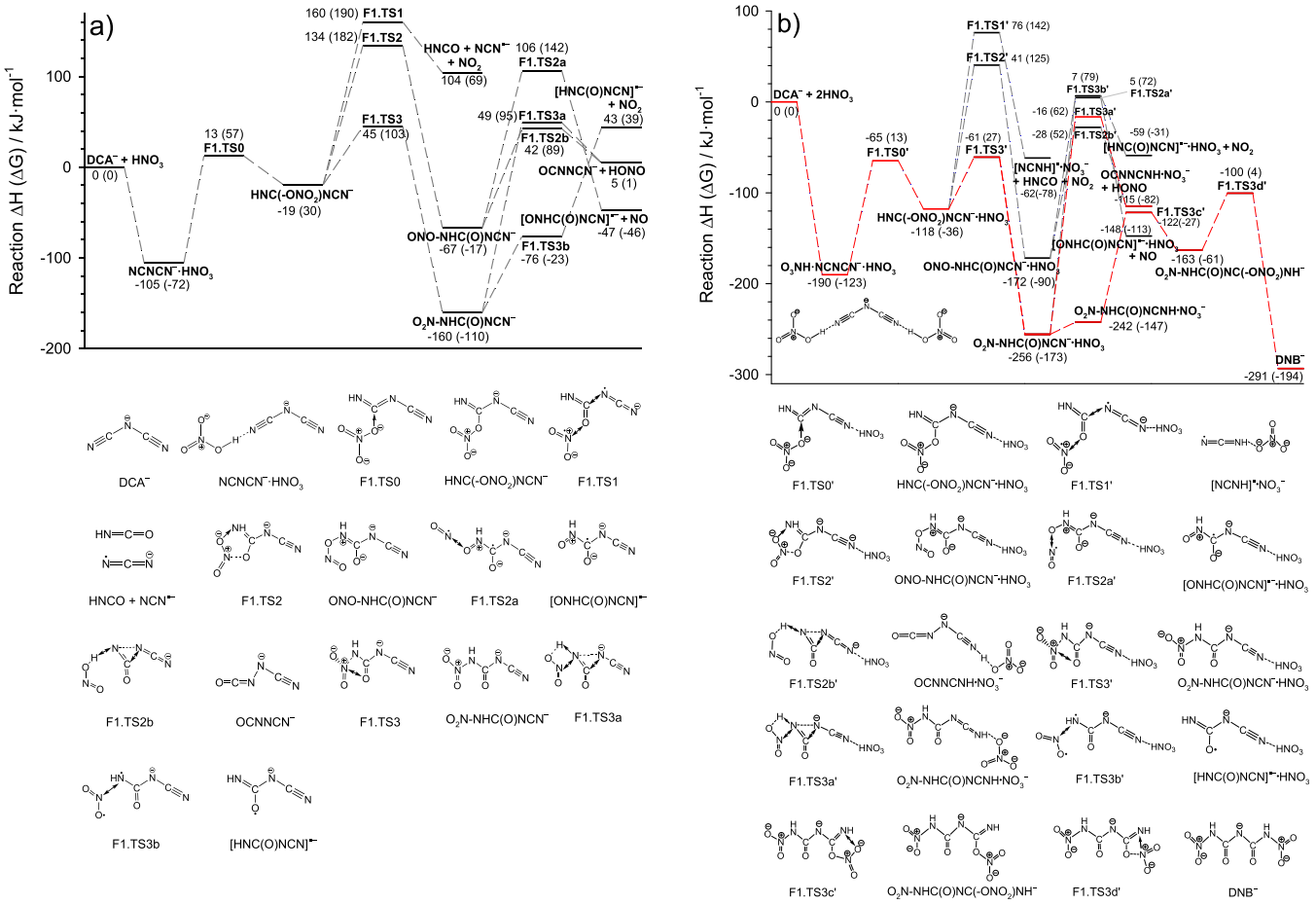

Figure 1. Reaction coordinates for the PT_{N1}-mediated reactions of DCA^- with (a) one and (b) two HNO_3. Structures and reaction ΔH (ΔG) at 298 K were calculated at the B3LYP/6-311++G(d,p) level of theory. Red-colored lines indicate the probable reaction pathways.

verified that PT_{N1} (*i.e.*, PT to a DCA^- terminal N) dominates as the primary reaction of DCA^- with HNO_3, forming a hydrogen-bonded complex $NCNCN^-{\cdot}HNO_3$. We have therefore explored reaction pathways that may evolve from this complex. Results are depicted in Figure 1a, with all of the structures and reaction ΔH and ΔG calculated at the B3LYP/6-311++G(d,p) level of theory. Consistent with the previous work,[6,18,22,23] the most favorable reaction pathway can be attributed to $DCA^- + HNO_3 \rightarrow NCNCN^-{\cdot}HNO_3 \rightarrow$ F1.TS0 $\rightarrow HNC(-ONO_2)NCN^- \rightarrow$ F1.TS3 $\rightarrow O_2N{-}NHC(O){-}NCN^-$. The latter may be followed by HONO elimination (*via* F1.TS3a) or NO_2 elimination (*via* F1.TS3b). Alternatively, the $HNC(-ONO_2)NCN^-$ intermediate may evolve to $ONO{-}NHC(O)NCN^-$ *via* F1.TS2, followed by NO elimination (*via* F1.TS2a) or HONO elimination (*via* F1.TS2b). As revealed in the trajectories, $HNC(-ONO_2)NCN^-$ is short-lived and decomposes to $[HNC(O)NCN]^{\bullet-} + NO_2$, and the product pair may recombine to form the $O_2N{-}NHC(O)NCN^-$ complex. $HNC(-ONO_2)NCN^-$ may also dissociate to $HNCO + NCN^{\bullet-} + NO_2$, which involves a high-energy barrier F1.TS1.

Considering that preignition is initiated in the condensed-phase IL solution wherein DCA^- is solvated by HNO_3, it is meaningful to examine the reactions of DCA^- with two HNO_3 molecules. One impact of adding a second HNO_3 to the reactants is that the formation of an additional hydrogen bond with DCA^- lowers the enthalpies and free energies of intermediate complexes and TSs and thus promotes downstream reactions (this is the same reason as that seen in the mixing of ILs and HNO_3 wherein the heat release from the hydrogen bond formation increases the temperature of the mixture[39]). The potential energy diagram for $DCA^- + 2HNO_3$ in Figure 1b demonstrates this point. All of the TSs in Figure 1b are labeled following the same numerical order as those in Figure 1a but are distinguished by a prime. Compared to the TSs with one HNO_3, the TSs for the same type of reaction but with two HNO_3 are lower in ΔH by 65−106 kJ/mol and in ΔG by 33−76 kJ/mol (the relatively small changes in ΔG are due to the entropic loss with the addition of a second HNO_3). Nearly all the intermediate complexes are stabilized to a similar extent as the corresponding TSs. The only exception is NO_2 elimination of $O_2N{-}NHC(O)NCN^-{\cdot}HNO_3$, in which the barrier F1.TS3b′ increases compared to F1.TS3b.

The most important consequence of having two HNO_3 react with DCA^- concerns the evolution of two exothermic product channels with no activation barriers above the reactants (highlighted in red in Figure 1b). The first one corresponds to $DCA^- + 2HNO_3 \rightarrow O_3NH{\cdot}NCNCN^-{\cdot}HNO_3 \rightarrow$ F1.TS0′ $\rightarrow HNC(-ONO_2)NCN^-{\cdot}HNO_3 \rightarrow$ F1.TS3′ $\rightarrow O_2N{-}NHC(O)NCN^-{\cdot}HNO_3 \rightarrow O_2N{-}NHC(O)NCNH{\cdot}NO_3^- \rightarrow$ F1.TS3c′ $\rightarrow O_2N{-}NHC(O)NC(-ONO_2)N^- \rightarrow$ F1.TS3d′ $\rightarrow DNB^-$, where both HNO_3 molecules are reacting with DCA^- rather than one acting as a spectator.[6,18] The second product channel is the dissociation of $O_2N{-}NHC(O)NCN^-{\cdot}HNO_3$ to $OCNNCNH{\cdot}NO_3^-$ (wherein the proton is shifted to the CN group) + HONO *via* F1.TS3a′. The dissociation

https://dx.doi.org/10.1021/acs.jpcb.0c07823
J. Phys. Chem. B 2020, 124, 11175−11188

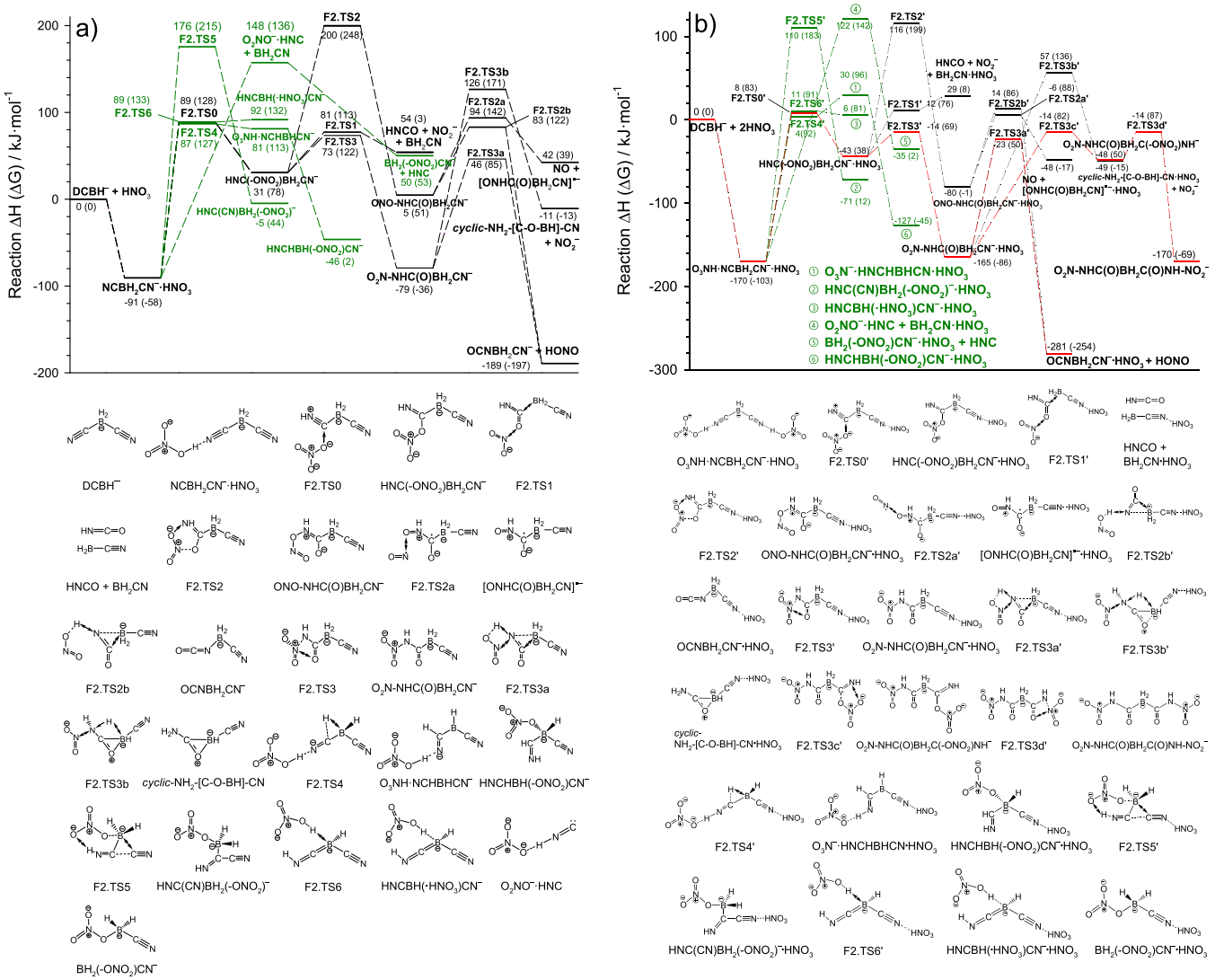

Figure 2. Reaction coordinates for the PT-mediated reactions of $DCBH^-$ with (a) one and (b) two HNO_3. Structures and reaction ΔH (ΔG) at 298 K were calculated at the B3LYP/6-311++G(d,p) level of theory. Green-colored lines indicate the BH_2-mediated reaction pathways, while red-colored lines indicate the probable reaction pathways.

requires a higher activation energy and thus is less competitive than the formation of DNB^-. This may explain the absence of HONO in the DCA^- ignition products.[6,18]

4.1.2. Reaction Pathways Initiated by PT_{N3}. A few trajectories of DCA^- + HNO_3 resulted in PT_{N3} (*i.e.*, PT to the central N in DCA^-), for which the reaction coordinate and energetics were mapped out in Figure S3a in the Supporting Information. It turns out that, following the formation of $(CN)_2N^-{\cdot}HNO_3$, the only feasible product channel is $[NC(O)NHCN]^{\bullet-}$ + NO_2. This pathway not only bears an activation ΔH (ΔG) of 115 (161) kJ/mol above the reactants but also is endothermic by 94 kJ/mol and endoergic by 86 kJ/mol in the products. Even with a second HNO_3, the additional hydrogen bond energy (see Figure S3b in the Supporting Information) is not sufficient to eliminate the reaction endothermicity.

4.1.3. Reaction Pathways Initiated by PT to a C Atom in DCA^-. Besides interacting with the DCA^- nitrogen atoms, the HNO_3 proton may react with a C atom in DCA^- (henceforth referred to as PT_{C2}). The resulting reaction coordinate is shown in Figure S4a in the Supporting In formation. However, the PT_{C2} activation barrier FS4.TS0 is located at ΔH (ΔG) of 246 (277) kJ/mol above the reactants; moreover, the resulting adduct *cyclic*-$CH(NO_3^-)NN(CN)$ has an endothermicity of 202 kJ/mol and endoergicity of 236 kJ/mol. This renders PT_{C2} and its downstream pathways insignificant. Indeed, no PT_{C2} reaction was observed in the trajectory simulations.

We have also investigated PT_{C2} in the presence of a second HNO_3 (see Figure S4b in the Supporting Information). While the second HNO_3 lowers reaction energies, the activation barriers FS4.TS0′ still bears a ΔH (ΔG) of 164 (232) kJ/mol with respect to the sum of DCA^- + $2HNO_3$, and the *cyclic*-$CH(NO_3^-)NN(CN{\cdot}HNO_3)$ product has a ΔH (ΔG) of 141 (210) kJ/mol.

4.2. Reaction of $DCBH^-$ with HNO_3. *4.2.1. Reaction Pathways Initiated by PT.* Guided by the trajectory results of $DCBH^-$ + HNO_3 and $HDCBH$ + NO_3^- and by the reaction mechanisms we have identified in its analogous system DCA^- + HNO_3, we may deduce reaction pathways for $DCBH^-$ + HNO_3. Similar to those for DCA^- + HNO_3, the trajectories for $DCBH^-$ + HNO_3 are dominated by PT to a terminal N in $DCBH^-$. Therefore, we explored in Figure 2a the reaction

https://dx.doi.org/10.1021/acs.jpcb.0c07823
J. Phys. Chem. B 2020, 124, 11175−11188

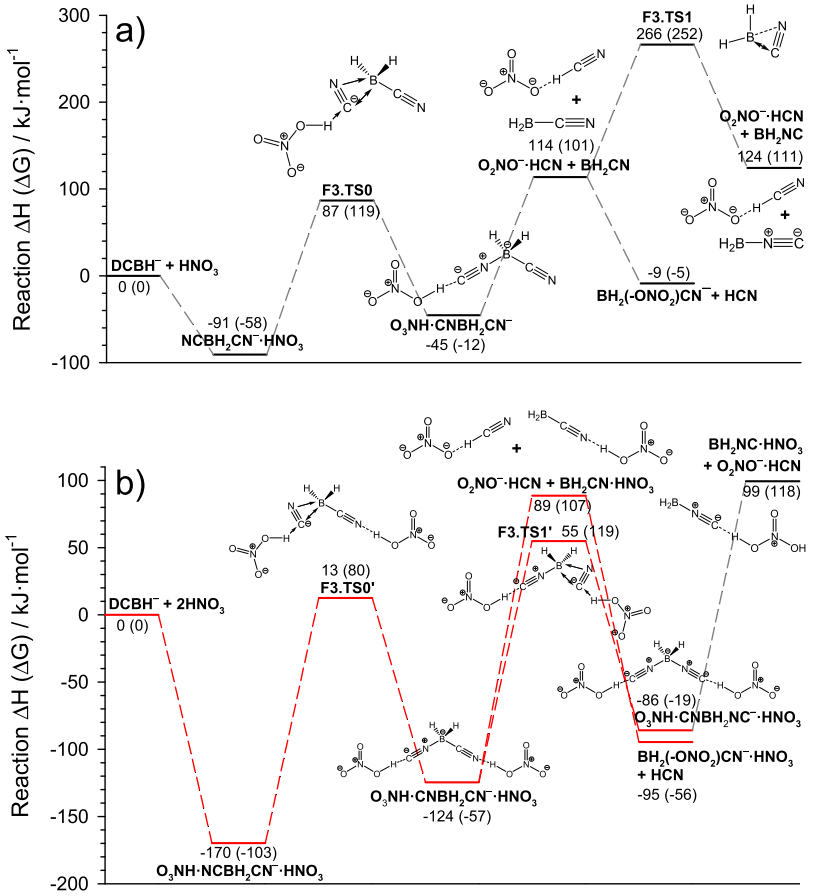

Figure 3. Reaction coordinates for the isomerization of $DCBH^-$ with (a) one and (b) two HNO_3. Structures and reaction ΔH (ΔG) at 298 K were calculated at the B3LYP/6-311++G(d,p) level of theory. Red-colored lines indicate the probable reaction pathways.

pathways that can be initiated by a terminal hydrogen-bonded $NCBH_2CN^-{\cdot}HNO_3$ complex. As shown in the figure, the black-colored pathways are all facilitated by an $HNC(-ONO_2)BH_2CN^-$ intermediate and cross over barriers at F2.TS1, TS2, TS2a, TS2b, TS3, and TS3a. These pathways are each analogues of the DCA^- reactions that are mediated by $HNC(-ONO_2)NCN^-$ and cross over F1.TS1, TS2, TS2a, TS2b, TS3, or TS3a (see Figure 1a), respectively. The only difference is that the NO_2 elimination of $HNC(-ONO_2)BH_2CN^-$ (*via* F2.TS3b) leads to *cyclic*-NH_2-[C−O−BH]-CN and NO_2^- anion (rather than a neutral NO_2 as in the reaction of DCA^-). Energetically, the $DCBH^-$ reactions are less favorable than the same type of reactions in $DCA^- + HNO_3$, as the formation barrier F2.TS0 (also the rate-limiting barrier) for $HNC(-ONO_2)BH_2CN^-$ is 76 (71) kJ/mol higher in ΔH (ΔG) than F1.TS0 for $HNC(-ONO_2)NCN^-$.

Besides the common reaction pathways as in DCA^-, $DCBH^-$ presents unique BH_2-mediated pathways (plotted by the green-colored lines in Figure 2a). These pathways start from the $NCBH_2CN^-{\cdot}HNO_3$ complex and proceed along F2.TS4 → $O_3NH{\cdot}NCHBHCN^-$ (*i.e.*, a 1,2-H shift), F2.TS5 → $HNC(CN)BH_2(-ONO_2)^-$ (*i.e.*, rearrangement), F2.TS6 → $HNCBH(\cdot HNO_3)CN^-$ (*i.e.*, PT), and $NCBH_2CN^-{\cdot}HNO_3$ → $O_2NO^-{\cdot}HNC + BH_2CN$ → $BH_2(-ONO_2)CN^- + HNC$, respectively.

Again, adding a second HNO_3 to the reaction enhances the $DCBH^-$ oxidation. It not only lowers reaction activation barriers and stabilizes intermediates but also leads to two exothermic product channels with no barriers above the reactants. These two product channels are featured by the red-colored lines in Figure 2b. The first channel follows $DCBH^- + 2HNO_3$ → $O_3NH{\cdot}NCBH_2CN^-{\cdot}HNO_3$ → F2.TS0′ → $HNC(-ONO_2)BH_2CN^-{\cdot}HNO_3$ → F2.TS3′ → $O_2N{-}NHC(O)BH_2CN^-{\cdot}HNO_3$ → F2.TS3c′ → $O_2N{-}NHC(O)BH_2C(-ONO_2)NH^-$ → F2.TS3d′ → $O_2N{-}NHC(O)BH_2C(O)NH{-}NO_2^-$. This channel bears a resemblance to the formation of DNB^- in $DCA^- + 2HNO_3$. The second channel deviates from the first one at $O_2N{-}NHC(O)BH_2CN^-{\cdot}HNO_3$ and leads to dissociation products $OCNBH_2CN^-{\cdot}HNO_3$ + HONO *via* F2.TS3a′, which is reminiscent of the production of $OCNNCNH{\cdot}NO_3^-$ + HONO in $DCA^- + 2HNO_3$.

4.2.2. $DCBH^-$ Isomerization. Unlike the high-activation barrier and thus inaccessible PT_{C2} in $DCA^- + HNO_3$, the attack of HNO_3 proton upon a C atom in $DCBH^-$ triggers a key reaction in that the $NC{-}BH_2$ bond breaks and in the meantime the terminal N starts to bond with boron. As a result, the NC group flips with respect to the boron and forms an isomer $O_3NH{\cdot}CNBH_2CN^-$. The reaction was identified by the trajectory in Figure S2d. Its potential energy diagram was constructed in Figure 3a with an activation ΔH (ΔG) of 87 (119) kJ/mol and the product ΔH (ΔG) of −45 (−12) kJ/mol.

The isomerization becomes more feasible upon the addition of a second HNO_3 (Figure 3b) and both of the two CN groups may flip, leading to the successive formation of $O_3NH{\cdot}CNBH_2CN^-{\cdot}HNO_3$ and $O_3NH{\cdot}CNBH_2NC^-{\cdot}HNO_3$ with the activation ΔH (ΔG) of 13 (80) kJ/mol for the first isomerization and of 55 (119) kJ/mol for the second. The

https://dx.doi.org/10.1021/acs.jpcb.0c07823
J. Phys. Chem. B 2020, 124, 11175−11188

bindings of HNO_3 with the C atoms in $O_3NH{\cdot}CNBH_2CN^-$, $O_3NH{\cdot}CNBH_2CN^-{\cdot}HNO_3$, and $O_3NH{\cdot}CNBH_2NC^-{\cdot}HNO_3$ are more alike an ion−dipole interaction and thus are weaker than the hydrogen bonding in $O_3NH{\cdot}NCBH_2NC^-$ and $O_3NH{\cdot}NCBH_2CN^-{\cdot}HNO_3$. The $O_3NH{\cdot}CNBH_2CN^-$, $O_3NH{\cdot}CNBH_2CN^-{\cdot}HNO_3$, and $O_3NH{\cdot}CNBH_2NC^-{\cdot}HNO_3$ isomers are able to continue on along the pathways depicted in Figure 3a,b to produce $BH_2(-ONO_2)CN^-/BH_2(-ONO_2)CN^-{\cdot}HNO_3$, $BH_2CN/BH_2CN{\cdot}HNO_3$, $BH_2NC/BH_2NC{\cdot}HNO_3$, and $HCN/O_2NO^-{\cdot}HCN$ fragments. The significance of these isomers will be further discussed below.

4.2.3. H_2 Elimination. The trajectories in Figures S2c,d have revealed two H_2-elimination pathways for $DCBH^- + HNO_3$. Their reaction coordinates are compared in Figure 4a. The

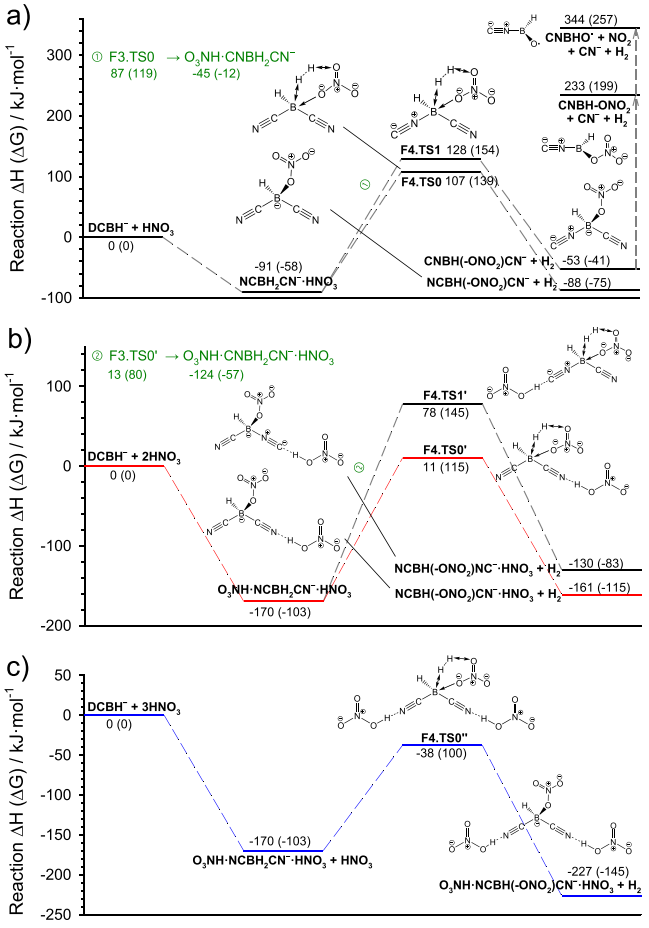

Figure 4. Reaction coordinates for the H_2 elimination of $DCBH^-$ with (a) one, (b) two, and (c) three HNO_3. Structures and reaction ΔH and ΔG at 298 K were calculated at the B3LYP/6-311++G(d,p) level of theory. Red-colored lines indicate the probable reaction pathways.

trajectory pathway of Figure S2c is governed by F4.TS0, and the resulting product pair of $NCBH(-ONO_2)CN^- + H_2$ produces a reaction exothermicity of 88 kJ/mol. The trajectory of Figure S2d reveals a more convoluted yet less energetically favorable pathway. The reaction is initiated by the isomerization of $NCBH_2CN^-{\cdot}HNO_3$ to $O_3NH{\cdot}CNBH_2CN^-$ *via* F3.TS0 (as described in Figure 3a), followed by H_2 elimination *via* F4.TS1. The resulting product ion $CNBH(-ONO_2)CN^-$ is less stable than $NCBH(-ONO_2)CN^-$ and may eliminate CN^- and NO_2 consecutively.

Both H_2-elimination pathways become more energetically favorable when a second HNO_3 is hydrogen bonded to $DCBH^-$. As shown by the potential energy diagram in Figure 4b, the ΔH (ΔG) for F4.TS0′ is 11 (115) kJ/mol versus 107 (139) kJ/mol for F4.TS0, and 78 (145) kJ/mol for F4.TS1′ versus 128 (154) kJ/mol for F4.TS1. To take a closer look at the H_2 elimination in $DCBH^- + 2HNO_3$, we mapped out in Figure 5 a 2D-PES along the reaction coordinates rHH and

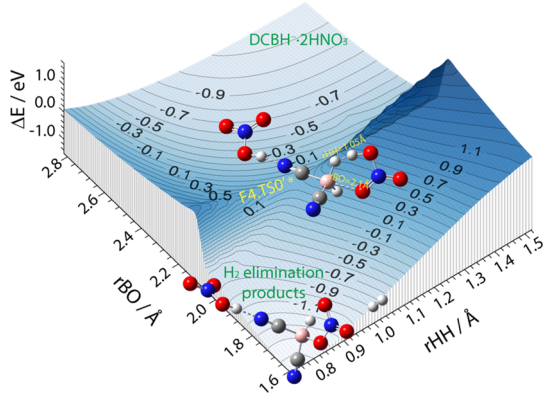

Figure 5. Two-dimensional PES for the H_2 elimination of $DCBH^-$ + $2HNO_3$. Electronic energy (ΔE with respect to starting reactants) was calculated at the B3LYP/6-311++G(d,p) level of theory.

rBO. rHH is the distance between the proton of HNO_3 and one hydride H of $DCBH^-$, which describes the formation of H_2. rBO is the distance between the B atom and an O atom of HNO_3, which follows the formation of $NCBH(-ONO_2)CN^-{\cdot}HNO_3$. The PES scanned rHH from 1.52 to 0.72 Å and rBO from 2.82 to 1.60 Å, with a step size of 0.05 Å for each. All of the other bond lengths and bond angles were optimized during PES scan. On this PES, there is only one barrier (*i.e.*, F4.TS0′) leading from the reactants to $NCBH(-ONO_2)CN^-{\cdot}HNO_3 + H_2$, which is located at rHH = 1.05 Å and rBO = 2.10 Å. This barrier represents the activation energy required for H_2 elimination. The surface leading from post-TS to the formation of the $NCBH(-ONO_2)CN^-{\cdot}HNO_3$ complex (*i.e.*, the region within rHH < 1.05 Å and rBO < 2.2 Å) becomes flat and descends slowly, indicating that the $-ONO_2$ addition is barrierless. It also suggests that H_2 elimination and formation of $NCBH(-ONO_2)CN^-{\cdot}HNO_3$ happen sequentially in the reaction of $DCBH^- + 2HNO_3$ rather than in a concerted way, which is consistent with the finding in the H_2-elimination trajectory for $DCBH^- + HNO_3$.

Finally, inspired by the importance of additional HNO_3 in the H_2 elimination, we have examined the H_2 elimination in the presence of three HNO_3 molecules. Results are indicated by the F4.TS0″-mediated pathway shown in Figure 4c. It was found that a third HNO_3 further reduces the reaction activation ΔH (ΔG) by 49 (15) kJ/mol at F4.TS0″ compared to F4.TS0′. In the meantime, the H_2-elimination products from $DCBH^- + 3HNO_3$ are more exothermic (by 66 kJ/mol) and exoergic (by 30 kJ/mol) than those of $DCBH^- + 2HNO_3$. Moreover, the third HNO_3 induces new H_2 elimination reactions of $O_3NH{\cdot}CNBH_2CN^-{\cdot}HNO_3 \rightarrow O_3NH{\cdot}CNBH(-ONO_2)CN^-{\cdot}HNO_3 + H_2$ and $O_3NH{\cdot}CNBH_2NC^-{\cdot}HNO_3 \rightarrow O_3NH{\cdot}CNBH(-ONO_2)NC^-{\cdot}HNO_3 + H_2$ (not shown in the figure).

https://dx.doi.org/10.1021/acs.jpcb.0c07823
J. Phys. Chem. B 2020, 124, 11175−11188

Table 3. Comparison of the Reaction Product Channels of DCA^- *vs* $DCBH^-$ with a Single HNO_3 (Energy Unit: kJ·mol^{-1}), Where the Probable Product Channels Are Highlighted in Bold

products	rate-limiting TS ΔH (ΔG)	product ΔH (ΔG)
PT_{N1}-initiated product channels of DCA^- + HNO_3		
$NCNCN^-{\cdot}HNO_3$	**none**	**−105 (−72)**
$HNC(-ONO_2)NCN^-$	**13 (57)**	**−19 (30)**
HNCO + $[NCN]^{\bullet-}$ + NO_2	160 (190)	104 (69)
ONO−NHC(O)NCN^-	134 (182)	−67 (−17)
$[ONHC(O)NCN]^{\bullet-}$ + NO	134 (182)	−47 (−46)
$OCNNCNH{\cdot}NO_3^-$ + HONO	45 (103)	5 (1)
O_2N−NHC(O)NCN^-	**45 (103)**	**−160 (−110)**
$[HNC(O)NCN]^{\bullet-}$ + NO_2	45 (103)	43 (39)
PT_{C2}-initiated product channels of DCA^- + HNO_3		
cyclic-$CH(NO_3^-)NN(CN)$	246 (277)	202 (236)
$O_2NONCHNCN^-$	246 (277)	97 (146)
$[ONCHNCN]^{\bullet-}$ + NO_2	246 (277)	155 (151)
$ONCH(ONO)NCN^-$	246 (277)	113 (156)
OCHNNCN + NO_2^-	325 (367)	142 (139)
$OCHN(NO_2)NCN^-$	325 (367)	33 (82)
$[ONNNCN]^{\bullet-}$ + $HCO_2^{\bullet}$	325 (367)	141 (135)
NO + $^{\bullet}NNCN$ + HCO_2^-	325 (367)	113 (62)
PT_{N3}-initiated product channels of DCA^- + HNO_3		
$(CN)_2N^-{\cdot}HNO_3$	**none**	**−90 (−51)**
$[NC(O)NHCN]^{\bullet-}$ + NO_2	115 (161)	94 (86)

products	rate-limiting TS ΔH (ΔG)	product ΔH (ΔG)
PT-initiated product channels of $DCBH^-$ + HNO_3		
$NCBH_2CN^-{\cdot}HNO_3$	**none**	**−91 (−58)**
$HNC(-ONO_2)BH_2CN^-$	89 (128)	31 (78)
HNCO + BH_2CN + NO_2^-	89 (128)	54 (3)
ONO−NHC(O)BH_2CN^-	200 (248)	5 (51)
$[ONHC(O)BH_2CN]^{\bullet-}$ + NO	200 (248)	42 (39)
$OCNBH_2CN^-$ + HONO	89 (128)	−189 (−197)
O_2N−NHC(O)BH_2CN^-	89 (128)	−79 (−36)
cyclic-NH_2−[C−O−BH]−CN + NO_2^-	126 (171)	−11 (−13)
$O_3NH{\cdot}NCHBHCN^-$	87 (127)	81 (113)
$HNCHBH(-ONO_2)CN^-$	87 (127)	−46 (2)
$HNC(CN)BH_2(-ONO_2)^-$	176 (215)	−5 (44)
$HNCBH(HNO_3)CN^-$	89 (133)	92 (132)
$O_2NO^-{\cdot}HNC$ + BH_2CN	none	148 (136)
$BH_2(-ONO_2)CN^-$ + HNC	148 (136)	50 (53)
Isomerization of $DCBH^-$		
$O_3NH{\cdot}CNBH_2CN^-$	87 (119)	−45 (−12)
$O_2NO^-{\cdot}HCN$ + BH_2CN	87 (119)	114 (101)
$O_2NO^-{\cdot}HCN$ + BH_2NC	266 (252)	124 (111)
$BH_2(-ONO_2)CN^-$ + HCN	**114 (101)**	**−9 (−5)**
H_2 elimination of $DCBH^-$ + HNO_3		
$NCBH(-ONO_2)CN^-$ + H_2	107 (139)	−88 (−75)
$CNBH(-ONO_2)CN^-$ + H_2	128 (154)	−53 (−41)
$CNBH{-}ONO_2$ + CN^- + H_2	none	233 (199)
$[CNBHO]^{\bullet}$ + NO_2 + CN^- + H_2	none	344 (257)

5. COMPARISON OF THE HNO_3-OXIDATION OF DCA^- VERSUS $DCBH^-$

5.1. Identification of Probable Product Channels. The trajectory simulations combined with the reaction coordinates and potential energy diagrams have revealed that the HNO_3 oxidation of $DCBH^-$ not only shares many similar primary and secondary reaction types and therefore produces many similar product structures as that of DCA^- but also presents unique chemistry owing to its boron-hydride group.

In both reaction systems, PT from HNO_3 to the reactant anion serves as an initial step. The secondary reactions between the proton-transferred products evolve into various product channels. The reaction data for DCA^- + HNO_3 and $DCBH^-$ + HNO_3 are compiled in Table 3, including ΔH and ΔG (with respect to starting reactants) for TSs and products. For a product channel that involves more than one TS, only the rate-limiting TS is listed. The pathways and products are grouped on the basis of their starting mechanisms and those of the same type in DCA^- + HNO_3 versus $DCBH^-$ + HNO_3 are listed side by side.

The motivation for our kinetics modeling is to decide which ones of these reaction pathways are able to prompt IL preignition. The identification of probable reaction pathways is based on two factors: reaction product enthalpy that determines whether the reaction is able to release heat and thus increases the system's temperature and reaction activation energy that determines whether the reaction is accessible in reality. While the reaction exothermicity can be calculated directly, the reaction activation energy required for probable pathways is less obvious. To this end, a quantitative criterion was set for TSs on the basis of experimental ID time. The ID time (τ) in the drop tests may be approximately treated in pseudo-first-order kinetics: $\tau = 1/k_{mixing} + 1/(k_{rxn}\cdot[IL])$ where k_{mixing} and k_{rxn} are the mixing and reaction rate constants, respectively.[9] The dynamics simulations of $BMIM^+DCA^-$ IL with HNO_3 revealed a quick mixing of the two liquids;[18] therefore, the lower limit of k_{rxn} may be estimated by $1/(\tau\cdot[IL])$. The fuel liquid number density is 3.2×10^{21} molecule/cm^3 as estimated from the IL density and molecular weight. Accordingly, an ID time of 50 ms at 573 K leads to a minimum k_{rxn} of 6.3×10^{-21} molecule^{-1}·cm^3·s^{-1}. Following $k_{rxn} = Ae^{-\Delta G^*/k_BT}$ (where A is 1×10^{-10} for typical IL-gas reactions,[9] k_B is the Boltzmann constant and T is the temperature), the corresponding activation free energy is 116 kJ/mol.

On the basis of the above analysis, all of the reaction pathways which have negative product ΔH and activation $\Delta G \leq 116$ kJ/mol are able to contribute to the preignition. These probable pathways are highlighted in bold in Table 3. For DCA^- + HNO_3, there are four probable products: $NCNCN^-{\cdot}HNO_3$, $(CN)_2N^-{\cdot}HNO_3$, $HNC(-ONO_2)NCN^-$, and O_2N−NHC(O)NCN^-. For $DCBH^-$ + HNO_3, only the formation of $NCBH_2CN^-{\cdot}HNO_3$ and $BH_2(-ONO_2)CN^-$ + HCN meets the criteria for a probable reaction.

As we have rationalized, a second HNO_3 enhances reactions and opens many new product channels in DCA^- + $2HNO_3$ and $DCBH^-$ + $2HNO_3$, as highlighted in Table 4. Such an

https://dx.doi.org/10.1021/acs.jpcb.0c07823
J. Phys. Chem. B 2020, 124, 11175−11188

Table 4. Comparison of the Reaction Product Channels of DCA^- *vs* $DCBH^-$ with Two HNO_3 Molecules (Energy Unit: kJ·mol^{-1}), Where the Probable Product Channels Are Highlighted in Bold

products	rate-limiting TS ΔH (ΔG)	product ΔH (ΔG)	products	rate-limiting TS ΔH (ΔG)	product ΔH (ΔG)
PT_{N1}-initiated product channels of $DCA^- + 2HNO_3$			PT-initiated product channels of $DCBH^- + 2HNO_3$		
$O_3NH{\cdot}NCNCN^-{\cdot}HNO_3$	**none**	**−190 (−123)**	**$O_3NH{\cdot}NCBH_2CN^-{\cdot}HNO_3$**	**none**	**−170 (−103)**
$HNC(-ONO_2)NCN^-{\cdot}HNO_3$	**−65 (13)**	**−118 (−36)**	**$HNC(-ONO_2)BH_2CN^-{\cdot}HNO_3$**	**8 (83)**	**−43 (38)**
$HNCO + NO_2 + [NCNH]^{\bullet}{\cdot}NO_3^-$	76 (142)	−62 (−78)	$HNCO + NO_2^- + BH_2CN{\cdot}HNO_3$	8 (83)	29 (8)
$ONO-NHC(O)NCN^-{\cdot}HNO_3$	41 (125)	−172 (−90)	$ONO-NHC(O)BH_2CN^-{\cdot}HNO_3$	116 (199)	−80 (−1)
$[ONHC(O)NCN]^{\bullet-}{\cdot}HNO_3 + NO$	41 (125)	−148 (−113)	$[ONHC(O)BH_2CN]^{\bullet-}{\cdot}HNO_3 + NO$	116 (199)	−48 (−17)
$OCNNCNH{\cdot}NO_3^- + HONO$	**−16 (62)**	**−115 (−82)**	**$OCNBH_2CN^-{\cdot}HNO_3 + HONO$**	**8 (83)**	**−281 (−254)**
$O_2N-NHC(O)NCN^-{\cdot}HNO_3$	**−61 (27)**	**−256 (−173)**	**$O_2N-NHC(O)BH_2CN^-{\cdot}HNO_3$**	**8 (83)**	**−165 (−86)**
$O_2N-NHC(O)NC(-ONO_2)NH^-$	**−61 (27)**	**−163 (−61)**	**$O_2N-NHC(O)BH_2C(-ONO_2)NH^-$**	**8 (83)**	**−48 (50)**
DNB^-	**−61 (27)**	**−291 (−194)**	**$O_2N-NHC(O)BH_2C(O)NH-NO_2^-$**	**8 (83)**	**−170 (−69)**
$[HNC(O)NCN]^{\bullet-}{\cdot}HNO_3 + NO_2$	7 (79)	−59 (−31)	*cyclic*-$NH_2-[C-O-BH]-CN{\cdot}HNO_3 + NO_2^-$	57 (136)	−49 (−15)
			$O_3N^-{\cdot}HNCHBHCN{\cdot}HNO_3$	4 (92)	30 (96)
			$HNCHBH(-ONO_2)CN^-{\cdot}HNO_3$	**30 (96)**	**−127 (−45)**
			$HNC(CN)BH_2(-ONO_2)^-{\cdot}HNO_3$	110 (183)	−71 (12)
			$HNCBH(HNO_3)CN^-{\cdot}HNO_3$	11 (93)	6 (81)
			$O_2NO^-{\cdot}HNC + BH_2CN{\cdot}HNO_3$	none	122 (142)
			$BH_2(-ONO_2)CN^-{\cdot}HNO_3 + HNC$	122 (142)	−35 (2)
PT_{C2}-initiated product channels of $DCA^- + 2HNO_3$			Isomerization of $DCBH^-$		
cyclic-$CH(NO_3^-)NN(CN{\cdot}HNO_3)$	164 (232)	141 (210)	**$O_3NH{\cdot}CNBH_2CN^-{\cdot}HNO_3$**	**13 (80)**	**−124 (−57)**
$O_2NONCHNCN^-{\cdot}HNO_3$	164 (232)	2 (83)	$O_2NO^-{\cdot}HCN + BH_2CN{\cdot}HNO_3$	none	89 (107)
$[ONCHNCN]^{\bullet-}{\cdot}HNO_3 + NO_2$	164 (232)	64 (93)	$O_3NH{\cdot}CNBH_2NC^-{\cdot}HNO_3$	55 (119)	−86 (−19)
$ONCH(ONO)NCN^-{\cdot}HNO_3$	164 (232)	10 (88)	$BH_2NC{\cdot}HNO_3 + O_2NO^-{\cdot}HCN$	55 (119)	99 (118)
$OCHNNCN{\cdot}HNO_3 + NO_2^-$	199 (277)	123 (149)	**$BH_2(-ONO_2)CN^-{\cdot}HNO_3 + HCN$**	**89 (107)**	**−95 (−56)**
$OCHN(NO_2)NCN^-{\cdot}HNO_3$	199 (277)	−67 (16)			
$[ONNNCN]^{\bullet-}{\cdot}HNO_3 + HCO2^{\bullet}$	199 (277)	52 (80)			
$NO + {}^{\bullet}NNCN{\cdot}HNO_3 + HCO_2^-$	199 (277)	95 (71)			
PT_{N3}-initiated product channels of $DCA^- + 2HNO_3$			H_2 elimination of $DCBH^- + 2HNO_3$		
$NCN(HNO_3)CN^-{\cdot}HNO_3$	**none**	**−171 (−90)**	**$NCBH(-ONO_2)CN^-{\cdot}HNO_3 + H_2$**	**11 (115)**	**−161 (−115)**
$[NC(O)NHCN]^{\bullet-}{\cdot}HNO_3 + NO_2$	41 (121)	8 (34)	$NCBH(-ONO_2)NC^-{\cdot}HNO_3 + H_2$	78 (145)	−130 (−83)

influence appears to be more profound in the oxidation of $DCBH^-$. Not only has $DCBH^- + 2HNO_3$ reproduced all of the probable reaction types that were identified in $DCA^- + 2HNO_3$ but prompted BH_2-specific pathways to the formation of $HNCHBH(-ONO_2)CN^-{\cdot}HNO_3$, $O_3NH{\cdot}CNBH_2CN^-{\cdot}HNO_3$, and $NCBH(-ONO_2)CN^-{\cdot}HNO_3 + H_2$. Our investigation of $DCBH^-$ with three HNO_3 molecules suggests that the solvation of anions with more HNO_3 molecules would further reduce activation free energies and increase reaction heat release.

5.2. Comparison with Experiments. In a previous work,[20] we had verified that many of the experimentally detected DCA^- hypergolic reaction products (*e.g.*, HNCO, N_2O, and NO_2) could be produced by the thermal decomposition of its preignition product $O_2N-NHC(O)-NCN^-$ and/or DNB^-. Herein, we focus on comparing the theoretical oxidation products of $DCBH^-$ (identified in the trajectories and/or inferred from the reaction coordinates) with the TGA–MS and infrared spectroscopic measurements of the thermal decomposition and hypergolic reaction of $BMIM^+DCBH^-$.[24]

The computational modeling has predicted both the neutral NO_2 and its anionic form in the HNO_3-oxidation of $DCBH^-$, such as NO_2 elimination from $CNBH-ONO_2$, and the formation of NO_2^- from the decomposition of $HNC(-ONO_2)BH_2CN^-{\cdot}(HNO_3)_{0,1}$ and $O_2N-NHC(O)BH_2CN^-{\cdot}(HNO_3)_{0,1}$. NO_2 may also be produced in the thermal decomposition of HNO_3 and/or $CNBH(-ONO_2)CN^-$. On the other hand, the experiment[24] had detected, in the gas phase, only neutral NO_2 in the reaction of $BMIM^+DCBH^-$ with HNO_3. NO_2^- might possibly form in the experiment but remained in the IL as it could not vaporize.

On the basis of the structural similarity between the DNB^- and $O_2N-NHC(O)BH_2C(O)NH-NO_2^-$ complexes, we assume that $O_2N-NHC(O)BH_2C(O)NH-NO_2^-$ may present some fragmentation patterns similar to DNB^- and produce an $HNNO_2H$ fragment.[20,40] $HNNO_2H$ can decompose to N_2O according to our previous dynamics simulations,[20,40] which accounts for the detection of N_2O in the hypergolic experiments of both DCA^- and $DCBH^-$.[24] Finally, HCN was detected in the experiment.[24] According to our calculations, HCN may be produced from the decomposition of $O_3NH{\cdot}CNBH_2CN^-$. Alternatively, HCN may form by PT between CN^- and HNO_3.

5.3. Kinetics Analysis. We have now pinpointed the probable preignition reaction pathways of DCA^- and $DCBH^-$. For $DCA^- + 2HNO_3$, F1.TS0′ represents a rate-limiting step which leads the reaction from $O_3NH{\cdot}NCNCN^-{\cdot}HNO_3$ to the formation of DNB^-. For $DCBH^- + 2HNO_3$, F2.TS0′ initiates the pathway from $O_3NH{\cdot}NCBH_2CN^-{\cdot}HNO_3$ to $O_2N-NHC(O)BH_2C(O)NH-NO_2^-$ and $OCNBH_2CN^-{\cdot}HNO_3 + HONO$, F3.TS0′ mediates $DCBH^-$ isomerization, and F4.TS0′ governs H_2 elimination.

To evaluate whether and how these probable pathways can account for the preignition kinetics, their rate constants were calculated using the RRKM theory[36] as

https://dx.doi.org/10.1021/acs.jpcb.0c07823
J. Phys. Chem. B 2020, 124, 11175−11188

Table 5. RRKM Results for the Reactions of DCA^- *vs* $DCBH^-$ with Two HNO_3 Molecules

Temperature	573 K (300 °C)	723 K (450 °C)	873 K (600 °C)	1023 K (750 °C)	1173 K (900 °C)
			$DCA^- + 2HNO_3$		
$E_{internal}$ (kJ·mol^{-1})	93	130	171	213	258
k_{DCA} (s^{-1})	2.4×10^5	1.1×10^6	4.0×10^6	1.2×10^7	3.0×10^7
			$DCBH^- + 2HNO_3$		
$E_{internal}$ (kJ·mol^{-1})	101	144	189	237	288
$k_{F2.TS0'}$ (s^{-1})	5.2	2.7×10^2	5.4×10^3	5.5×10^4	3.5×10^5
$k_{F3.TS0'}$ (s^{-1})	1.1×10^2	7.5×10^3	1.7×10^5	2.0×10^6	1.3×10^7
$k_{F4.TS0'}$ (s^{-1})	1.0×10^2	7.2×10^3	2.0×10^5	2.5×10^6	1.9×10^7
$k_{DCBH^-} = \Sigma k_i$	2.15×10^2	1.5×10^4	3.75×10^5	4.5×10^6	3.3×10^7
$k_{F2.TS0'}/k_{F3.TS0'}/k_{F4.TS0'}$	2:51:47	2:50:48	1:46:53	1:43:56	1:40:59
k_{DCBH^-}/k_{DCA^-}	<0.01	0.014	0.1	0.4	1.1
			$DCBH^- + 3HNO_3$		
k_{DCBH^-} (s^{-1})	4.3×10^5	4.6×10^6	3.8×10^7	2.0×10^8	7.5×10^8
k_{DCBH^-}/k_{DCA^-}	1.8	4.2	10	17	25

$$k(E, J) = \frac{d}{h}\frac{\sum_{K=-J}^{J} G[E - E_0 - E_r^{\dagger}(J, K)]}{\sum_{K=-J}^{J} N[E - E_r(J, K)]}$$

where d is the reaction path degeneracy, G is the sum of states from 0 to $E - E_0 - E_r^{\dagger}$ at TS, N is the density of states of the energized reactant complex, E is the system energy, E_0 is the TS activation energy, E_r and $E_r^{\dagger}$ are the rotational energies of the complex and the TS, and J and K are the rotational quantum numbers for a symmetric top molecule. K was treated as active,[41] so that all $(2J + 1)$ K-levels were counted in $k(E,J)$. Calculations were done with the RRKM program of Zhu and Hase[37] using direct state count algorithm. Energies, vibrational frequencies, and moments of inertia of the complexes and TSs were obtained from the B3LYP/6-311++G(d,p) calculations.

Table 5 summarizes the RRKM results for $DCA^- + 2HNO_3$ and $DCBH^- + 2HNO_3$, which includes rate constants, branching ratios $(k_i/\Sigma k_i)$ among multiple product channels and the ratios of k_{DCBH^-}/k_{DCA^-} at different temperatures. The RRKM calculations predict that at lower temperatures, $DCBH^-$ reacts with HNO_3 slower than DCA^-, that is, the ratio of k_{DCBH^-}/k_{DCA^-} is less than 0.01 at 300 °C, increasing to 0.1 at 600 °C and 0.4 at 750 °C. However, k_{DCBH^-} exceeds k_{DCA^-} starting at 900 °C. In contrast to the exclusive formation of DNB^- in $DCA^- + 2HNO_3$, the $O_2N{-}NHC(O)BH_2C(O){-}NH{-}NO_2^-$ (and $OCNBH_2CN^-{\cdot}HNO_3$ + HONO) products are minor in $DCBH^- + 2HNO_3$, and H_2 elimination instead represents the most important product channel at all temperatures.

The kinetics for the H_2 elimination of $DCBH^-$ is further enhanced by reacting with three HNO_3 molecules, wherein two HNO_3 molecules are hydrogen bonded to the $DCBH^-$ terminal N atoms and the third one reacts with boron-hydride directly. With the participation of the third HNO_3, the H_2-elimination activation barrier (*i.e.*, F4.TS0″ in Figure 4c) decreases by 49 kJ/mol relative to F4.TS0′, and the H_2 elimination product channel becomes overwhelmingly dominant with a branching ratio of ≥98%. Consequently, k_{DCBH^-} is comparable to k_{DCA^-} at room temperature, becoming a factor of 2 higher than k_{DCA^-} at 300 °C and 1 order of magnitude higher at 600 °C and above.

The significance of H_2 elimination lies in the fact that the reactions are both strongly exothermic and exoergic, wherein the enthalpy and energy release prompt further reactions. Moreover, the H_2 product itself is an important fuel in rocket propulsion applications.[42] All of these may contribute to the enhanced preignition performance of $DCBH^-$ over DCA^-.

5.4. Reactions in Condensed-Phase ILs. Finally, in order to explore the changes of reaction profiles and energetics in the condensed-phase IL, we have calculated the probable reaction pathways using the SMD-GIL//B3LYP/6-311++G(d,p) method. The surrounding IL solvation shell was defined as ε (static dielectric constant of the solvent) = 11.5, n^2 (dynamic dielectric constant) = 2.0449, α (H bond acidity) = 0.229, β (H bond basicity) = 0.265, γ (surface tension at interface) = 61.24, φ (carbon aromaticity) = 0.2308, and ψ (electronegative halogenicity) = 0.0000.[43]

Figure 6a compares the reactions of $DCA^- + 2HNO_3$ in the condensed-IL (blue-colored lines) and in the gas phase (black-colored lines). All of the pathways follow similar reaction coordinates in the two different phases. However, the reaction potential energies change dramatically as indicated by green-colored lines. ΔHs (ΔGs) of TSs shift up from the gas phase to the condensed phase by an average of 68 (72) kJ/mol. The increases in the energies of intermediate complexes are even larger and depend on how many HNO_3 molecules are hydrogen bonded. For example, the ΔH (ΔG) of the reactant-like complex $O_3NH{\cdot}NCNCN^-{\cdot}HNO_3$ (with two hydrogen bonds) moves up by 110 (117) kJ/mol in the condensed IL. The ΔH (ΔG) of the nitro-complex $O_2N{-}NHC(O)NCN^-{\cdot}HNO_3$ (with one hydrogen bond) shifts by 86 (90) kJ/mol in the condensed phase. After both HNO_3 molecules are incorporated into the covalent structure of DNB^-, the difference between the gas-phase and the condensed-phase ΔH (ΔG) is only 61 (60) kJ/mol. A similar finding was reported by Chambreau *et al.*,[18] who compared $DCA^- + 2HNO_3$ in the gas phase versus in the condensed IL using the SMD-GIL//M06/6-31+G(d,p) level of theory.

We also compared the gas- and condensed-phase reactions of $DCBH^- + 2HNO_3$. Figure 6b1 shows the PT-initiated pathway, wherein the activation ΔG changes by 41−87 kJ/mol and the complex ΔH changes by 48−122 kJ/mol between the two phases. Figure 6b2,b3 shows $DCBH^-$ isomerization and H_2 elimination, respectively. As most reaction intermediates and products along these two pathways involve two hydrogen bonds, the differences between their gas- and condensed-phase ΔHs (ΔGs) are greater than 90 kJ/mol except those for $BH_2(-ONO_2)CN^-{\cdot}HNO_3$ + HCN and $NCBH(-ONO_2)CN^-{\cdot}HNO_3$ + H_2 wherein one HNO_3 has already been incorporated into a covalent structure.

https://dx.doi.org/10.1021/acs.jpcb.0c07823
J. Phys. Chem. B 2020, 124, 11175−11188

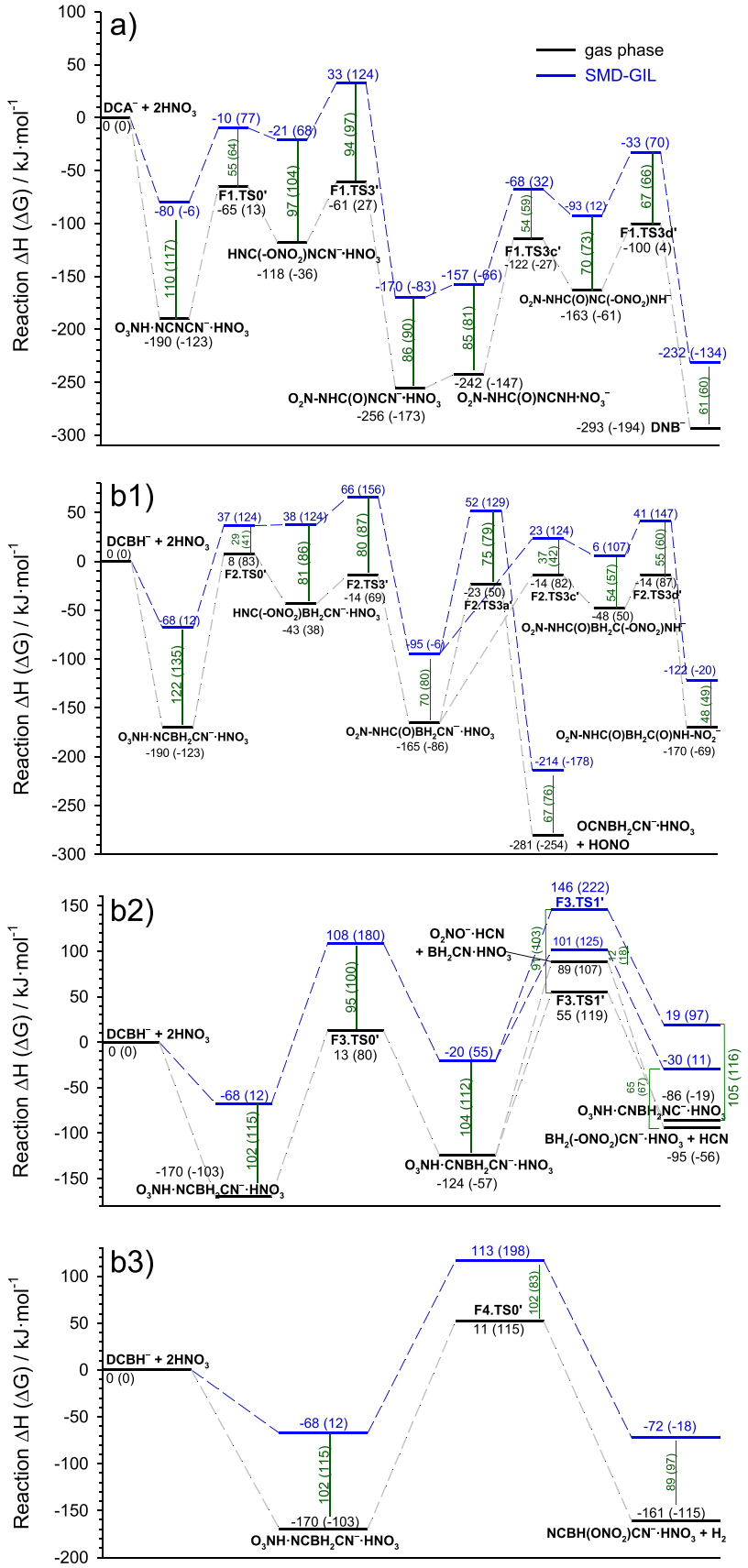

Figure 6. Comparison of gas- and condensed-phase reactions of (a) $DCA^- + 2HNO_3$ and (b) $DCBH^- + 2HNO_3$. Gas-phase results were calculated at B3LYP/6-311++G(d,p), and condensed-phase results were calculated at SMD-GIL//B3LYP/6-311++G(d,p).

https://dx.doi.org/10.1021/acs.jpcb.0c07823
J. Phys. Chem. B 2020, 124, 11175−11188

It appears from this that the number of hydrogen bonds in the reacting structures is a key factor that results in the significant difference between the gas-phase and SMD-GIL-calculated reaction energies. It was assumed that HNO_3 perturbs the solvation shell of the polar liquid solvent surrounding the anionic reactants. As a result, the SMD-GIL stabilizes the separated anions and HNO_3 more than the other points on the reaction PESs.[18] However, despite the energy shifts, the HNO_3 oxidation of DCA^- and $DCBH^-$ was found to follow the exact same reaction coordinates in the condensed-phase IL as in the gas phase. Therefore, the relative reactivities of DCA^- versus $DCBH^-$ should present the same trend in the two phases.

6. CONCLUSIONS

In the present work, direct dynamics trajectory simulations were carried out to probe reaction pathways and products in the HNO_3 oxidation of DCA^- and $DCBH^-$. Following trajectory predictions, reaction potential energy diagrams and surfaces were calculated in the gas and condensed phases. It was found that the most probable reaction pathways for the oxidation of DCA^- correspond to the formation of $O_2N-NHC(O)NCN^-$ and DNB^-. The HNO_3-oxidation of $DCBH^-$ shares many similar pathways as those of DCA^- and therefore produces similar products (*i.e.*, $O_2N-NHC(O)BH_2CN^-$ and $O_2N-NHC(O)BH_2C(O)NH-NO_2^-$). However, these DCA^--like pathways and products do not dominate the preignition process of $DCBH^-$. Instead, the preignition of $DCBH^-$ with HNO_3 occurs mostly as a result of the boron-hydride-specific reactions, of which the most important one is the elimination of H_2 *via* the combination of a hydride in the $DCBH^-$ and the proton in HNO_3. The statistical kinetics analysis suggests that H_2 elimination becomes overwhelmingly dominant when $DCBH^-$ reacts with multiple HNO_3 molecules, and the resulting phenomenological oxidation rate constant of $DCBH^-$ is an order of magnitude higher than that of DCA^-. The combination of fast reaction rate constants, large exothermicities of H_2 elimination, the high heat of combustion of the H_2 product, and the low viscosity of the $DCBH^-$–ILs have resulted in a shortened ID time and enhanced preignition performance of $DCBH^-$ over DCA^-. The present kinetics modeling has captured the distinctive preignition chemistry of $DCBH^-$ and DCA^- and rationalized the different HNO_3 oxidation kinetics of the two ILs. The key reactions of boron-hydride we have pinpointed in hypergolic preignition suggest the design of new IL anions toward enhanced H_2 elimination capabilities.

■ ASSOCIATED CONTENT

Supporting Information

The Supporting Information is available free of charge at https://pubs.acs.org/doi/10.1021/acs.jpcb.0c07823.

Representative trajectories, PT_{N3} and PT_{C2} reaction coordinates of DCA^- with HNO_3, and Cartesian coordinates for the calculated structures (PDF)

Videos for representative trajectories (ZIP)

■ AUTHOR INFORMATION

Corresponding Author

Jianbo Liu − *Department of Chemistry and Biochemistry, Queens College and the Graduate Center of the City University of New York, Queens, New York 11367, United States;* orcid.org/0000-0001-9577-3740; Phone: 1-718-997-3271; Email: jianbo.liu@qc.cuny.edu

Authors

Wenjing Zhou − *Department of Chemistry and Biochemistry, Queens College and the Graduate Center of the City University of New York, Queens, New York 11367, United States*

Steven D. Chambreau − *Jacobs, Inc., Air Force Research Laboratory, Edwards AFB, California 93524, United States*

Ghanshyam L. Vaghjiani − *In-Space Propulsion Branch, Rocket Propulsion Division, Aerospace Systems Directorate, Air Force Research Laboratory, AFRL/RQRS, Edwards AFB, California 93524, United States;* orcid.org/0000-0001-7473-7388

Complete contact information is available at: https://pubs.acs.org/10.1021/acs.jpcb.0c07823

Notes

The authors declare no competing financial interest.

■ ACKNOWLEDGMENTS

This work was supported by the Air Force Research Laboratory through ERC Inc., Subcontract no. PS170079, the Air Force Office of Scientific Research under Contract no. FA 9300-06-C-0023, and the Air Force Research Laboratory Faculty Summer Fellowship Program in 2019. W.Z. acknowledges the Queens College George Axelrad Research Award. The authors acknowledge the computer time provided by the High Performance Computing Center at the AFRL Department of Defense Research Center and thank Dr. Jerry Boatz (AFRL/RQRP) for valuable discussions regarding quantum chemistry approaches.

■ REFERENCES

(1) Zhang, Q.; Shreeve, J. n. M. Energetic Ionic Liquids as Explosives and Propellant Fuels: A New Journey of Ionic Liquid Chemistry. *Chem. Rev.* **2014**, *114*, 10527−10574.

(2) Schneider, S.; Hawkins, T.; Ahmed, Y.; Rosander, M.; Hudgens, L.; Mills, J. Green Bipropellants: Hydrogen-Rich Ionic Liquids that Are Hypergolic with Hydrogen Peroxide. *Angew. Chem., Int. Ed.* **2011**, *50*, 5886−5888.

(3) McCrary, P. D.; Chatel, G.; Alaniz, S. A.; Cojocaru, O. A.; Beasley, P. A.; Flores, L. A.; Kelley, S. P.; Barber, P. S.; Rogers, R. D. Evaluating Ionic Liquids as Hypergolic Fuels: Exploring Reactivity from Molecular Structure. *Energy Fuels* **2014**, *28*, 3460−3473.

(4) Liu, J.; Zhou, W.; Chambreau, S. D.; Vaghjiani, G. L. Molecular Dynamics Simulations and Product Vibrational Spectral Analysis for the Reactions of NO_2 with 1-Ethyl-3-methylimidazolium Dicyanamide ($EMIM^+DCA^-$), 1-Butyl-3-methylimidazolium Dicyanamide ($BMIM^+DCA^-$) and 1-Allyl-3-methylimidazolium Dicyanamide ($AMIM^+DCA^-$). *J. Phys. Chem. B* **2020**, *124*, 4303−4325.

(5) Liu, J.; Zhou, W.; Chambreau, S. D.; Vaghjiani, G. L. Computational Study of the Reaction of 1-Methyl-4-amino-1,2,4-triazolium Dicyanamide with NO_2: From Reaction Dynamics to Potential Surfaces, Kinetics and Spectroscopy. *J. Phys. Chem. B* **2019**, *123*, 2956−2970.

(6) Chambreau, S. D.; Schneider, S.; Rosander, M.; Hawkins, T.; Gallegos, C. J.; Pastewait, M. F.; Vaghjiani, G. L. Fourier Transform Infrared Studies in Hypergolic Ignition of Ionic Liquids. *J. Phys. Chem. A* **2008**, *112*, 7816−7824.

(7) Schneider, S.; Hawkins, T.; Rosander, M.; Vaghjiani, G.; Chambreau, S.; Drake, G. Ionic Liquids as Hypergolic Fuels. *Energy Fuels* **2008**, *22*, 2871−2872.

(8) Zhang, Y.; Shreeve, J. n. M. Dicyanoborate-Based Ionic Liquids as Hypergolic Fluids. *Angew. Chem., Int. Ed.* **2011**, *50*, 935−937.
(9) Thomas, A.; Chambreau, S. D.; Vaghjiani, G. L. Ignition Delay Reduction with Sodium Addition to Imidazolium-Based Dicyanamide Ionic Liquid. *J. Phys. Chem. A* **2019**, *123*, 10−14.
(10) Li, S.; Gao, H.; Shreeve, J. n. M. Borohydride Ionic Liquids and Borane/Ionic-Liquid Solutions as Hypergolic Fuels with Superior Low Ignition-Delay Times. *Angew. Chem., Int. Ed.* **2014**, *53*, 2969−2972.
(11) Zhang, Q.; Yin, P.; Zhang, J.; Shreeve, J. n. M. Cyanoborohydride-Based Ionic Liquids as Green Aerospace Bipropellant Fuels. *Chem.—Eur. J.* **2014**, *20*, 6909−6914.
(12) Liu, T.; Qi, X.; Huang, S.; Jiang, L.; Li, J.; Tang, C.; Zhang, Q. Exploiting Hydrophobic Borohydride-Rich Ionic Liquids as Faster-Igniting Rocket Fuels. *Chem. Commun.* **2016**, *52*, 2031−2034.
(13) Weng, X.; Tang, C.; Li, J.; Zhang, Q.; Huang, Z. Coulomb Explosion and Ultra-Fast Hypergolic Ignition of Borohydride-Rich Ionic Liquids with WFNA. *Combust. Flame* **2018**, *194*, 464−471.
(14) Li, X.; Lu, T.; Nan, J.; Li, H.; Nie, F.; Zhang, Y.-Q.; Chen, F.-X. Hydrophobic Hydrolytic-Stable N-Alkylimidazole-Cyanoborane Complexes as Ultrafast-Igniting Hypergolic Fuels. *ChemistrySelect* **2018**, *3*, 2548−2552.
(15) Jiao, N.; Zhang, Y.; Liu, L.; Shreeve, J. n. M.; Zhang, S. Hypergolic Fuels Based on Water-Stable Borohydride Cluster Anions with Ultralow Ignition Delay Times. *J. Mater. Chem. A* **2017**, *5*, 13341−13346.
(16) Bhosale, V. K.; Karnik, S.; Kulkarni, P. S. Ignition Study of Amine Borane/Cyanoborane Based Green Hypergolic Fuels. *Combust. Flame* **2019**, *210*, 1−8.
(17) Catoire, L.; Chambreau, S. D.; Vaghjiani, G. L. Chemical Kinetics Interpretation of Hypergolicity of Dicyanamide Ionic Liquid-Based Systems. *Combust. Flame* **2012**, *159*, 1759−1768.
(18) Chambreau, S. D.; Koh, C. J.; Popolan-Vaida, D. M.; Gallegos, C. J.; Hooper, J. B.; Bedrov, D.; Vaghjiani, G. L.; Leone, S. R. Flow-Tube Investigations of Hypergolic Reactions of a Dicyanamide Ionic Liquid via Tunable Vacuum Ultraviolet Aerosol Mass Spectrometry. *J. Phys. Chem. A* **2016**, *120*, 8011−8023.
(19) Geith, J.; Holl, G.; Klapötke, T. M.; Weigand, J. J. Pyrolysis Experiments and Thermochemistry of Mononitrobiuret (MNB) and 1,5-Dinitrobiuret (DNB). *Combust. Flame* **2004**, *139*, 358−366.
(20) Liu, J.; Chambreau, S. D.; Vaghjiani, G. L. Thermal Decomposition of 1,5-Dinitrobiuret (DNB): Direct Dynamics Trajectory Simulations and Statistical Modeling. *J. Phys. Chem. A* **2011**, *115*, 8064−8072.
(21) Litzinger, T.; Iyer, S. Hypergolic Reaction of Dicyanamide-Based Fuels with Nitric Acid. *Energy Fuels* **2011**, *25*, 72−76.
(22) Nichols, C. M.; Wang, Z.-C.; Yang, Z.; Lineberger, W. C.; Bierbaum, V. M. Experimental and Theoretical Studies of the Reactivity and Thermochemistry of Dicyanamide: $N(CN)_2^-$. *J. Phys. Chem. A* **2016**, *120*, 992−999.
(23) Vogelhuber, K. M.; Booth, R. S.; Annesley, C. J. Theoretical Investigation of the Reactivity of Sodium Dicyanamide with Nitric Acid. *J. Phys. Chem. A* **2018**, *122*, 1954−1959.
(24) Thomas, A. E.; Chambreau, S. D.; Redeker, N. D.; Esparza, A. A.; Shafirovich, E.; Ribbeck, T.; Sprenger, J. A. P.; Finze, M.; Vaghjiani, G. L. Thermal Decomposition and Hypergolic Reaction of a Dicyanoborohydride Ionic Liquid. *J. Phys. Chem. A* **2020**, *124*, 864−874.
(25) Brotton, S. J.; Kaiser, R. I. Controlled Chemistry via Contactless Manipulation and Merging of Droplets in an Acoustic Levitator. *Anal. Chem.* **2020**, *92*, 8371−8377.
(26) Liu, J.; Chambreau, S. D.; Vaghjiani, G. L. Dynamics Simulations and Statistical Modeling of Thermal Decomposition of 1-Ethyl-3-methylimidazolium Dicyanamide and 1-Ethyl-2,3-dimethylimidazolium Dicyanamide. *J. Phys. Chem. A* **2014**, *118*, 11133−11144.
(27) Döntgen, M.; Przybylski-Freund, M.-D.; Kröger, L. C.; Kopp, W. A.; Ismail, A. E.; Leonhard, K. Automated Discovery of Reaction Pathways, Rate Constants, and Transition States Using Reactive Molecular Dynamics Simulations. *J. Chem. Theory Comput.* **2015**, *11*, 2517−2524.
(28) Pratihar, S.; Ma, X.; Homayoon, Z.; Barnes, G. L.; Hase, W. L. Direct Chemical Dynamics Simulations. *J. Am. Chem. Soc.* **2017**, *139*, 3570−3590.
(29) Ma, X.; Hase, W. L. Perspective: Chemical Dynamics Simulations of Non-Statistical Reaction Dynamics. *Philos. Trans. R. Soc., A* **2017**, *375*, 20160204.
(30) Hase, W. L.; Bolton, K.; de Sainte Claire, P.; Duchovic, R. J.; Hu, X.; Komornicki, A.; Li, G.; Lim, K.; Lu, D.; Peslherbe, G. H.; et al. *VENUS 99: A General Chemical Dynamics Computer Program*; Texas Tech University: Lubbock, TX, 1999.
(31) Bakken, V.; Millam, J. M.; Bernhard Schlegel, H. Ab Initio Classical Trajectories on The Born-Oppenheimer Surface: Updating Methods for Hessian-Based Integrators. *J. Chem. Phys.* **1999**, *111*, 8773−8777.
(32) Frisch, M. J.; Trucks, G. W.; Schlegel, H. B.; Scuseria, G. E.; Robb, M. A.; Cheeseman, J. R.; Scalmani, G.; Barone, V.; Mennucci, B.; Petersson, G. A.; et al. *Gaussian 09*, Revision D.01; Gaussian, Inc: Wallingford, CT, 2013.
(33) Peslherbe, G. H.; Wang, H.; Hase, W. L. Monte Carlo Sampling for Classical Trajectory Simulations. *Adv. Chem. Phys.* **1999**, *105*, 171−201.
(34) Frisch, M. J.; Trucks, G. W.; Schlegel, H. B.; Scuseria, G. E.; Robb, M. A.; Cheeseman, J. R.; Scalmani, G.; Barone, V.; Petersson, G. A.; Nakatsuji, H.; et al. *Gaussian 16*, Revision B.01; Gaussian, Inc: Wallingford, CT, 2016.
(35) Alecu, I. M.; Zheng, J.; Zhao, Y.; Truhlar, D. G. Computational Thermochemistry: Scale Factor Databases and Scale Factors for Vibrational Frequencies Obtained from Electronic Model Chemistries. *J. Chem. Theory Comput.* **2010**, *6*, 2872−2887.
(36) Marcus, R. A. Unimolecular Dissociations and Free Radical Recombination Reactions. *J. Chem. Phys.* **1952**, *20*, 359−364.
(37) Zhu, L.; Hase, W. L. *A General RRKM Program (QCPE 644), Quantum Chemistry Program Exchange*; Chemistry Department, University of Indiana: Bloomington, 1993.
(38) Marenich, A. V.; Cramer, C. J.; Truhlar, D. G. Universal Solvation Model Based on Solute Electron Density and on a Continuum Model of the Solvent Defined by the Bulk Dielectric Constant and Atomic Surface Tensions. *J. Phys. Chem. B* **2009**, *113*, 6378−6396.
(39) Hooper, J. B.; Smith, G. D.; Bedrov, D. Thermophysical Properties of Energetic Ionic Liquids/Nitric Acid Mixtures: Insights from Molecular Dynamics Simulations. *J. Chem. Phys.* **2013**, *139*, 104503.
(40) Sun, R.; Siebert, M. R.; Xu, L.; Chambreau, S. D.; Vaghjiani, G. L.; Lischka, H.; Liu, J.; Hase, W. L. Direct Dynamics Simulation of the Activation and Dissociation of 1,5-Dinitrobiuret (HDNB). *J. Phys. Chem. A* **2014**, *118*, 2228−2236.
(41) Zhu, L.; Hase, W. L. Comparison of Modes for Calculating the RRKM Unimolecular Rate Constant k(E,J). *Chem. Phys. Lett.* **1990**, *175*, 117−124.
(42) Dawson, V. P.; Bowles, M. D. *Taming Liquid Hydrogen: The Centaur Upper Stage Rocket 1958−2002*; US National Aeronautics and Space Admin, 2004.
(43) Bernales, V. S.; Marenich, A. V.; Contreras, R.; Cramer, C. J.; Truhlar, D. G. Quantum Mechanical Continuum Solvation Models for Ionic Liquids. *J. Phys. Chem. B* **2012**, *116*, 9122−9129.

https://dx.doi.org/10.1021/acs.jpcb.0c07823
J. Phys. Chem. B 2020, 124, 11175−11188